Bachelor Thesis

Magnetic Flux Quanta in High-T_c / Low-T_c Superconducting Rings with π-phase-shifts

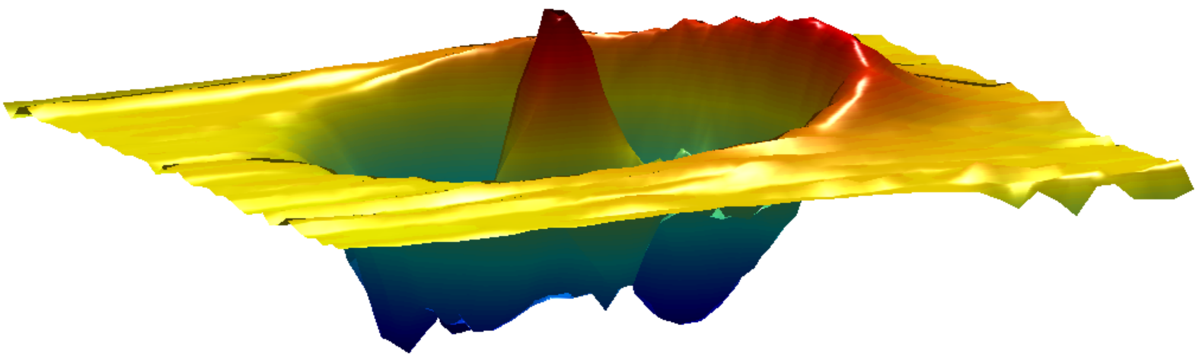

Robin Bruel
André Timmermans

June 2013

Supervisor:
Prof. dr. ir. J.W.M. Hilgenkamp

Work performed at:
Interfaces and Correlated Electron systems group
TNW Faculty
University of Twente
P.O. Box 217
7500 AE Enschede

Summary

This thesis was made as part of a bachelor project on the experimental observation of the ±1½ magnetic flux quantum (Φ_0 = 2.07 · 10^{-15} Wb) state in a specific type of superconducting rings, known as π-rings. The main reason for our research on this topic is the fact that the ±1½Φ_0 state has not been measured in superconducting structures so far, while in theory there is no reason why it cannot be measured.

The superconducting rings used in our research are partly made of a high critical temperature superconductor, yttrium barium copper oxide (YBCO), and partly made of a low critical temperature superconductor, niobium (Nb).

Indeed, the ±1½Φ_0 state in a π-ring has been observed in our measurements performed within an external magnetic field and in our measurements performed without an external magnetic field. The magnetic flux through the superconducting rings as a function of increasing external magnetic field is expected to increase in discrete steps with a size of the magnetic flux quantum Φ_0. These discrete steps have also been measured in our in-field measurements and in our zero-field measurements. The discrete steps are positioned differently for the so called 0- and π-rings.

The measurements that have been performed to observe these discrete steps are done using scanning SQUID microscopy (SSM). The reason why the SSM measurement setup is used is mainly the high sensitivity of the Superconducting Quantum Interference Device (SQUID). Another advantage is that the SSM measurement setup is able to scan rather large sample surface areas, so several YBCO/Nb rings can be scanned.

The significance of the research performed in this project lies both in verifying the theoretical expectations of flux quantization and in practical applications of flux quantization. The fact that we have measured the 0Φ_0, ±½Φ_0, ±1Φ_0, ±1½Φ_0 and 2Φ_0 states in our superconducting loops gives rise to the expectation that higher integer and higher half-integer numbers of magnetic flux quanta can also be captured in superconducting loops. The only limitation to this is the height of the supercurrent that can flow through these rings without exceeding the critical current of the Josephson junctions in the loop. Applications of these results will mostly be in the field of superconducting digital electronics and especially quantum-electronics.

Contents

Chapter 1. Introduction

In past research, for example by dr. J.R. Kirtley, dr. C.C. Tsuei *et al.* [1], the state of a superconducting ring demonstrating a spontaneously generated magnetic flux corresponding to +1½ or -1½, shortly ±1½, magnetic flux quantum Φ_0, has never been measured. Since, theoretically, there is no reason so far why the ±1½Φ_0 state in such a ring would not be possible, it was proposed by dr. C.C. Tsuei that this state should be searched for and observed experimentally.

In previous research on the influence of the angle between two high-T_c/low-T_c Josephson junctions that are placed in a superconducting YBCO/Nb ring, several states with quantized magnetic flux both higher and lower than |±1½Φ_0| have been observed [1]. The goal of our research is to either measure the ±1½Φ_0 state in a superconducting π-ring or prove that it does not exist.

The outline of the thesis is as follows: in chapter 2, the theory concerning superconductivity and magnetic flux quantization will be discussed. The chapter will start with an overview of some important topics in superconductivity. After this the fluxoid quantization condition for both integer and half-integer flux quanta is derived. Eventually, some theoretical background on the working of the used scanning SQUID microscope (SSM) setup is given. Also here, the reader will be introduced to the program that is used to derive the current density in the scanned rings on the sample from the magnetic flux measurements.

Chapter 3 deals with the more experimental aspects of this project. The devices that are used will be covered and the experimental realization of the sample will be explained.

Chapter 4 concerns the results of the performed measurements. The measurement data is given in the form of several graphs. The results are separated between measurements performed without an external magnetic field and with an external magnetic field when measuring. In this chapter, the hypothesis for the measurements of the quantized magnetic flux states in the 0- and π-ring as a function of the applied magnetic field during the cool-down of the sample will also be given.

In chapter 5, the results shown in chapter 4 will be discussed. First, the results will be compared to the hypothesis. Thereafter, the results will be compared to each other. Possible experimental errors in the measured values of parameters and the resulting possible error in the magnetic flux values will be taken into account in this chapter.

In chapter 6, the results and the discussions will be interpreted. The physical meaning of the processed data is discussed and conclusions are drawn. At the end, there will be an advice on possible future research in the topic of magnetic flux quanta in high-T_c/low-T_c superconducting rings with π-phase-shifts.

In this thesis, magnetic field is denoted by both symbols B and H. The vector field $\mathbf{B}$ is used in theoretical reasoning where it stands for the magnetic flux density. The vector field $\mathbf{H}$ denotes the magnetizing field or auxiliary magnetic field in more practical situations. So both $\mathbf{B}$ and $\mathbf{H}$ stand for a magnetic field. $\mathbf{B}$ has the unit tesla (T) and $\mathbf{H}$ has the unit ampere per meter (A/m) in the SI system. The unit for magnetic flux Φ, which is the integral of magnetic field over an area, is the weber (Wb = Tm^2). In the CGS system of units, the unit of $\mathbf{B}$ is gauss (G). For the gauss is used as the unit for magnetic field in experimental environments like ours, the gauss will be used as the unit for magnetic field strength in chapters 4 and 5, 'Results' and 'Discussion' respectively, in this thesis. The gauss unit is practical because one gauss unit denotes a very small magnetic flux density compared to one tesla unit; and in the experiments conducted in this thesis, very small magnetic field variations in the order of magnitude of mG = 10^{-3} G = 10^{-7} T, are externally applied on our sample using a solenoid. The gauss-tesla conversion is very straightforward: G = 10^{-4} T.

Chapter 2. Theoretical aspects

2.1. Introduction

The following chapter will cover the theory used in this thesis. First, superconductivity in general will be covered. Important properties, such as the Meissner effect, will be explained. The second part will focus on superconducting ring structures and especially the integer and half-integer quantization of magnetic flux through these structures. This flux quantization condition will be derived by using the single-valuedness of the so called order parameter wave function, which is explained in section 2.2. After this, some theory is explained on the topic of SQUIDs. A SQUID is the measurement device that is used for the measurements performed during this project. A more detailed description of the scanning SQUID microscopy (SSM) setup is given in chapter 3.

At the end of this chapter, a program will be introduced that is able to derive the current density in the scanned rings on the sample from the magnetic flux measurements using only one spatial component of the magnetic field.

An alternative derivation of half-integer flux quantization by means of energy minimization is given in appendix A. This derivation might also give a more intuitive grasp of the spontaneous current that is generated to induce the half flux quantum.

2.2 Superconductivity

There are two important ways to classify superconductors. The most straightforward way is to divide all superconducting materials into groups by their critical temperature, T_c. If the temperature of a superconductor is below its critical temperature, the material enters a superconductive state. The critical temperature can be used to divide all superconductors into a group with a critical temperature below 30 K, called low-T_c superconductors, and a group with a critical temperature above 30 K, called high-T_c superconductors.

Another way to classify superconductors is by the possibility of a magnetic field penetrating the superconductor. Type I superconductors are superconductors with one critical external magnetic field, H_c. Above this magnetic field the superconductor is in its normal state and magnetic field can penetrate the superconductor as it can penetrate any other non-superconducting material. Below this magnetic field the superconductor is in its superconductive state and it will completely shield the bulk of the superconductor from magnetic fields.

There are also type II superconductors. This type has two critical external magnetic fields, H_{c1} and H_{c2}. This type of superconductor knows three regimes. If $H < H_{c1} < H_{c2}$ the superconductor is in its superconductive state. This regime is exactly the same as a type I superconductor in an applied external magnetic field below its critical value.

The second regime is observed when $H > H_{c2} > H_{c1}$. In this regime the superconductor is in its normal state in the same way as a type I superconductor in an applied external magnetic field above H_c.

The third regime is found when $H_{c1} < H < H_{c2}$. This is called the intermediate state. In the intermediate state the magnetic field is allowed to partially penetrate the superconductor. Parts of the superconductor that are penetrated by the magnetic field will be in their normal state, and currents will circulate around these regions. Such circulating currents are called *vortices*.

The type I and type II superconductors do not only have critical external magnetic fields, but they also have a critical temperature. The critical magnetic field, H_c for a type I and H_{c1} or H_{c2} for a type II superconductor, is always a function of temperature.

When the critical temperature T_c is reached, $H_c(T) = H_c(T_c) = 0$ and the superconductor will always be in its normal state. Characteristic phase diagrams for type I and type II superconductors are shown in figure 2.1.

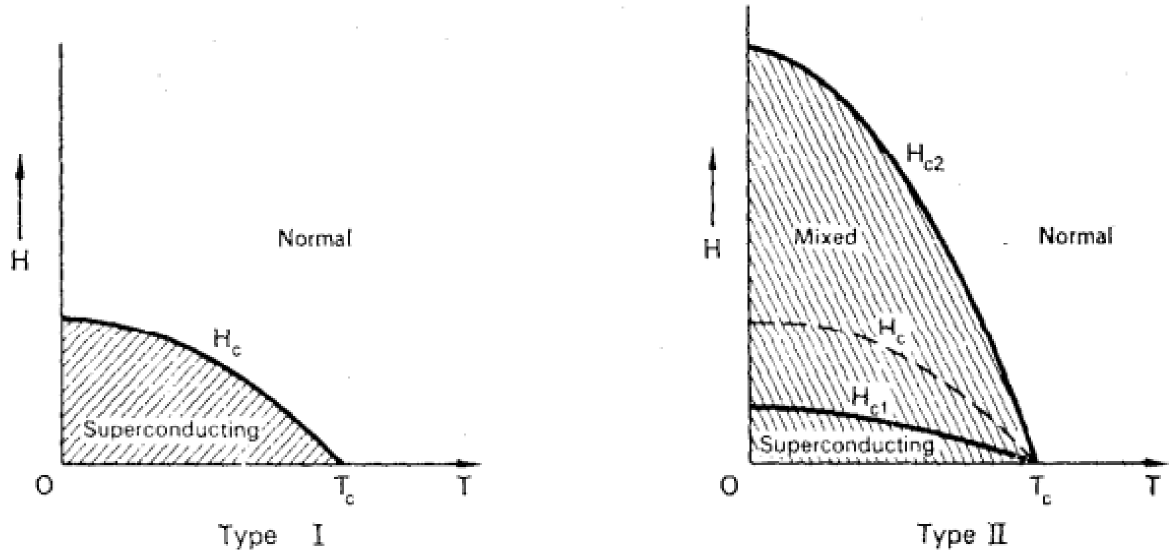

Figure 2.1: The left figure shows the phase diagram of a type I superconductor. The curve $H_c(T)$ is shown. Every state that is above this line is in its normal, non-superconductive, state. However, every state below the line is in its superconductive state. When the temperature hits the critical temperature T_c, there is no superconductive state and the material will always be in its normal state. The right figure shows the phase diagram for a type II superconductor as a solid line. When a state is between $H_{c1}(T)$ and $H_{c2}(T)$ the material is in its intermediate or mixed state, where the magnetic field is able to penetrate the material and form vortices. Below H_{c1} and above H_{c2} are the superconductive and normal state respectively. For comparison, the phase diagram of a type I superconductor is shown as a dashed line (figure adapted from Tinkham [2]).

In this thesis, superconductors will mostly be classified as being either high-T_c superconductors or low-T_c superconductors. This is because of the fundamentally different nature of these two groups of superconductors. This different nature is the cause of some interesting properties that are observed when high-T_c superconductors and low-T_c superconductors are brought in contact. Furthermore, the superconductors on which the rings used in the experiments are based, yttrium barium copper oxide (YBCO) and niobium (Nb), are both type II superconductors. So no distinction can be made with respect to the type I/II classification.

Since the discovery of superconductivity by Heike Kamerlingh Onnes in 1911, a lot of research has been conducted in this topic. Both experimentally, with results like the discovery of high-T_c superconductivity [3], and theoretically, like the explanation of low-T_c superconductivity. The theoretical explanation of low-T_c superconductivity was given in 1957 by Bardeen, Cooper and Schrieffer [4, 5]. They were awarded the Noble Prize in Physics for their *BCS-Theory* in 1972 [6]. According to the BCS theory, the charge carriers are bound into so called *Cooper pairs* via interactions with the lattice of the material, called electron-phonon interactions. While unbound electrons behave as fermions and are subjected to the Pauli exclusion principle, these Cooper pairs behave as bosons and are all able to occupy the same state. This state has an energy gap with respect to the next state. Even though BCS-theory has provided an explanation for low-T_c superconductivity, high-T_c superconductivity is still unexplained.

In 1930, Meissner and Ochsenfeld discovered the *Meissner-Ochsenfeld effect*, usually shortened to simply the *Meissner effect*. The Meissner effect is the expulsion of magnetic field from a superconducting material when this material enters its superconductive state [7], as shown in figure 2.2.

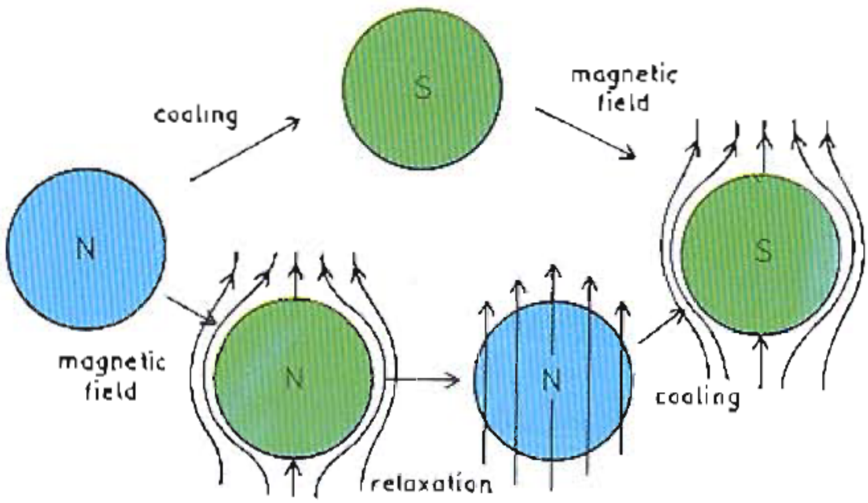

Figure 2.2: This figure shows a schematic picture of the Meissner effect. When a normal metal without superconducting properties (N) is exposed to a magnetic field, the magnetic field is expulsed by currents generated in the material. These currents quickly die out after some time due to resistance. When this material now enters the superconductive state (S), the magnetic field is expulsed again by generated *shielding currents*. These shielding currents do not die out after a given time because of the resistanceless conduction of the superconductor. This gives rise to the Meissner effect [7] (figure adapted from Ginzburg, Andryushin [8]).

Though both high-T_c and low-T_c superconductors show the Meissner effect and are resistanceless when in their superconductive state, there is a great difference between the two. Both types of superconductors are described by their own so called *order parameter* Ψ. This order parameter Ψ can be interpreted as the quantum mechanical wave function of the superconductor as a whole. The squared modulus $|\Psi|^2$ is a measure for the number of electrons in the superconductive state. The order parameter is different for low-T_c and high-T_c superconductors.

As an example niobium and YBCO, the two important superconductors central to this thesis, are compared. Niobium is a low-T_c superconductor. Its order parameter is a so called s-wave. On the other hand, the high-T_c superconductor YBCO has a $d_{x^2-y^2}$ order parameter. A schematic drawing of these order parameters is shown in figure 2.3. The effects resulting from this difference in order parameter will be discussed in section 2.3 and especially starting from 2.3.3.

Figure 2.3: In this figure, blue lobes represent positive values, while red lobes represent negative values. The signs can be arbitrarily chosen as long as there is a minus sign difference between the two. The left figure shows an s-wave order parameter wave function. This wave function is always positive. The right figure shows a $d_{x^2-y^2}$-wave function. This wave function has both positive and negative lobes. If the two were to be combined together, this would imply a phase-shift of π in the order parameter wave function because of the different sign between the lobe of the $d_{x^2-y^2}$- and s-wave [9] (figure adapted from Verwijs [9]).

2.3. Integer and fractional flux quantization

2.3.1 Magnetic flux quantization

The Cooper pairs that are all in the same quantum mechanical state are called the *condensate*. The condensate in the superconducting system can be described as a single wave function

$$\Psi(\mathbf{r},t) = |\Psi(\mathbf{r},t)|e^{i\theta(\mathbf{r},t)} \tag{2.1}$$

Here $\Psi(\mathbf{r},t)$ is the quantum mechanical wave function, $|\Psi(\mathbf{r},t)|$ is the amplitude of the wave function and $\theta(\mathbf{r},t)$ is the phase of the wave function at position $\mathbf{r}$ and time t. The *macroscopic wave function* (2.1) as shown above has to obey the time-dependent Schrödinger equation [10]

$$\left[\frac{1}{2m}\left(\frac{\hbar}{i}\nabla - q\mathbf{A}\right)^2 + q\phi\right]\Psi = i\hbar\frac{\partial\Psi}{\partial t} \tag{2.2}$$

with m the mass of the Cooper pairs, q the charge of the Cooper pairs, $\mathbf{A}(\mathbf{r},t)$ the magnetic vector potential and $\phi(\mathbf{r},t)$ the scalar potential. These potentials are related to the magnetic and electric fields $\mathbf{B}$ and $\mathbf{E}$ by

$$\mathbf{B} = \nabla \times \mathbf{A} \tag{2.3}$$

and

$$\mathbf{E} = -\nabla\phi - \frac{\partial\mathbf{A}}{\partial t} \tag{2.4}$$

respectively.

If equation (2.2) is multiplied by Ψ^* and its complex conjugate is subtracted, we find

$$-\nabla\cdot\left[\frac{\hbar}{2mi}(\Psi^*\nabla\Psi - \Psi\nabla\Psi^*) - \frac{q}{m}|\Psi|^2\mathbf{A}\right] = \frac{\partial}{\partial t}(\Psi^*\Psi) \tag{2.5}$$

Multiplying equation (2.5) by q we obtain the electromagnetic continuity equation

$$\frac{\partial\rho_s}{\partial t} = -\nabla\cdot\mathbf{J}_s \tag{2.6}$$

with ρ_s the charge density and

$$\mathbf{J}_s = \frac{\hbar q}{2mi}(\Psi^*\nabla\Psi - \Psi\nabla\Psi^*) - \frac{q^2}{m}|\Psi|^2\mathbf{A} \tag{2.7}$$

the current density. Equation (2.7) is known as the second Ginzburg-Landau equation named after the first to derive it by expanding the free energy of a superconductor in powers of Ψ [11].

Substituting equation (2.1) into equation (2.7) results in

$$\frac{m}{nq^2}\mathbf{J}_s + \mathbf{A} = \frac{\hbar}{q}\nabla\theta \tag{2.8}$$

where n is the local charge carrier density in the superconducting condensate. To obtain this result it is assumed that $\Psi^*\Psi$ can be interpreted as n because the number of charge carriers involved in the superconducting condensate is large. Integrating equation (2.8) around a closed contour Γ yields

$$\frac{\hbar}{q}\oint_\Gamma \nabla\theta\cdot d\mathbf{l} = \oint_\Gamma \frac{m}{nq^2}\mathbf{J}_s\cdot d\mathbf{l} + \oint_\Gamma \mathbf{A}\cdot d\mathbf{l} = \frac{m}{nq^2}\oint_\Gamma \mathbf{J}_s\cdot d\mathbf{l} + \Phi \tag{2.9}$$

Here equation (2.3) and Stokes' Theorem have been invoked to identify the magnetic flux

$$\oint_\Gamma \mathbf{A}\cdot d\mathbf{l} = \int_S (\nabla\times\mathbf{A})\cdot d\mathbf{S} = \int_S \mathbf{B}\cdot d\mathbf{S} \equiv \Phi \tag{2.10}$$

The wave function introduced in equation (2.1) has to be single-valued. This yields the condition that integrating $\nabla\theta$ over a closed contour has to yield a multiple of 2π. Implementing this condition in equation (2.9) results in the fluxoid quantization condition:

$$\frac{m}{nq^2}\oint_\Gamma \mathbf{J}_s \cdot d\mathbf{l} + \Phi = \frac{h}{q}\mathrm{n} = \mathrm{n}\Phi_0, \mathrm{n}\epsilon\mathbb{Z} \tag{2.11}$$

in which

$$\Phi_0 \equiv \frac{h}{|q|} = \frac{h}{2e} = 2.07 \cdot 10^{-15}\ \mathrm{Wb} \tag{2.12}$$

is the *magnetic flux quantum*.

In the bulk of a superconductor, magnetic field is expelled by the Meissner effect[7]. Because of this effect it is impossible for a current to flow in the bulk of the superconductor. If one defines the closed integration path Γ to be in the bulk of the superconductor where the current density $\mathbf{J}_s$ is zero, we find, by equation (2.11), that the flux in the enclosed hole is quantized

$$\Phi = \mathrm{n}\Phi_0, \mathrm{n}\epsilon\mathbb{Z} \tag{2.13}$$

In 1961 the effect of flux quantization was experimentally observed by Deaver and Fairbank. This proved not only that the flux through a superconducting loop is quantized, but also that the charge carriers in a superconductor carry a charge of $q = -2e$ as expected from the BCS-theory, where electrons bond in Cooper pairs [12]. It is important to note that equation (2.13) is a special case. In general, the *fluxoid*, defined as the left-hand side of equation (2.11), is quantized, not the flux. Another important aspect is that Φ stands for the total flux, which is a sum of the externally applied flux and the self-generated flux.

2.3.2 Gauge invariance

The vector- and scalar potentials $\mathbf{A}$ and ϕ are defined by the partial differential equations (2.3) and (2.4). The results from these equations are not unique. These equations are invariant under the *gauge transformation* [13]

$$\begin{aligned} \mathbf{A} &\rightarrow \mathbf{A} + \nabla\chi \\ \phi &\rightarrow \phi - \frac{\partial\chi}{\partial t} \end{aligned} \tag{2.14}$$

Simply combining the gauge transformations (2.14) with equation (2.8) suggests that the supercurrent density $\mathbf{J}_s$ is dependent on the gauge chosen for $\mathbf{A}$ and ϕ. However, j_s is a quantity that can be experimentally measured, so it is impossible that it is dependent on the gauge that is chosen in (2.14). This problem can be fixed by noting that the Schrödinger equation (2.2) is still gauge invariant when the phase θ is transformed along with $\mathbf{A}$ and ϕ as

$$\theta \rightarrow \theta - \frac{2\pi}{\Phi_0}\chi \tag{2.15}$$

If this transformation is done along with the transformations in (2.14), $\mathbf{J}_s$ is again independent of the chosen gauge.

2.3.3 Josephson junctions

A Josephson junction is a weak link between two superconductors. The weak link can, in general, consist of an insulating barrier, a small region of non-superconducting material or a physical barrier that weakens superconductivity in some region. In the Josephson junction the macroscopic wave functions of the two superconductors overlap. This overlap can create a phase jump in the total wave function that gives rise to a current across the Josephson junction. If no magnetic field is present, the current flowing through the junction is related to the phase drop between the two wave functions via [14]

$$I_s = I_c \sin(\theta_1 - \theta_2)_{\mathbf{A}=\mathbf{0}} \tag{2.16}$$

Here I_s is the current in the superconductor, $\theta_1 - \theta_2$ is the phase difference between the overlapping order parameter wave functions and I_c is the critical current of the junction. The critical current is the maximum current that can flow through the Josephson junction without losing the superconductivity in the junction. The phase terms θ_1 and θ_2 will depend on the gauge chosen in equation (2.15). Equation (2.16) can be written in a gauge invariant way by defining the gauge such that

$$\mathbf{A}' = \mathbf{A} + \nabla\chi = \mathbf{0} \tag{2.17}$$

where $\mathbf{A}'$ is the gauge invariant magnetic vector potential. Using this gauge we obtain the phase difference

$$\theta_1' - \theta_2' = \theta_1 - \theta_2 + \frac{2\pi}{\Phi_0}\int_{\mathbf{r}_1}^{\mathbf{r}_2} \nabla\chi \cdot d\mathbf{l} \tag{2.18}$$

Using $I_s = I_s' = I_c \sin(\theta_1' - \theta_2')_{\mathbf{A}'=\mathbf{0}}$ together with (2.17) and (2.18) we find

$$I_s = I_c \sin\varphi \tag{2.19}$$

with φ the *gauge invariant phase difference*, defined by

$$\varphi \equiv \theta_1 - \theta_2 - \frac{2\pi}{\Phi_0}\int_{\mathbf{r}_1}^{\mathbf{r}_2} \mathbf{A} \cdot d\mathbf{l} \tag{2.20}$$

2.3.4 Magnetic flux quantization in loops with junctions

Let us consider a loop containing N Josephson junctions. Magnetic flux quantization in such a loop is again dictated by the single-valuedness of the macroscopic wave function in the superconductor. Using equations (2.8) and (2.20) the flux through a loop becomes

$$\oint \nabla\theta \cdot d\mathbf{l} = -\frac{2\pi}{\Phi_0}\int_{\Gamma'} \frac{m}{nq^2}\mathbf{J}_s \cdot d\mathbf{l} - \frac{2\pi}{\Phi_0}\oint \mathbf{A} \cdot d\mathbf{l} - \sum_{i=1}^{N} \varphi_i \tag{2.21}$$

In this equation the contour Γ' is a contour in the bulk of the superconducting loop, as in the derivation of equation (2.13), but with the Josephson junctions excluded. Because of our choice of the integration path and the Meissner effect we can assume that $\mathbf{J}_s$ is zero as we have done to get to equation (2.13)[7]. The single-valuedness of the wave function and Stokes' Theorem now simplify (2.21) to the fluxoid quantization condition for loops containing N Josephson junctions

$$\Phi + \frac{\Phi_0}{2\pi}\sum_{i=1}^{N} \varphi_i = \mathrm{n}\Phi_0, \mathrm{n}\epsilon\mathbb{Z} \tag{2.22}$$

This equation shows that the sum of the flux and normalized phase is quantized.

2.3.5 π Josephson junctions in superconducting loops

A π Josephson junction is a Josephson junction where the gauge invariant phase difference $\varphi = \pi$. The effect of a π Josephson junction in a loop is shown in the fluxoid quantization condition for loops with a π-phase-shift. Assuming we have a loop containing two junctions, one with $\varphi_1 = \pi$ and one with $\varphi_2 = 0$, we can use equation (2.22) to find the flux through the superconducting loop:

$$\Phi + \frac{\Phi_0}{2\pi}\sum_{i=1}^{2}\varphi_i = \mathrm{n}\Phi_0 \rightarrow \Phi = \left(\mathrm{n} + \frac{1}{2}\right)\Phi_0, \mathrm{n}\epsilon\mathbb{Z} \tag{2.23}$$

This result implies that the magnetic flux through the loop is not simply quantized to an integer multiple of Φ_0. Instead, it is quantized to an integer multiple of Φ_0 and offset by ½Φ_0. Would the phase shifts in the junction have been $\varphi_1 = \varphi_2 = 0$ or $\varphi_1 = \varphi_2 = \pi$ the result would have been the same as equation (2.13). Concluding, the π-phase-shift results in a half flux quantum offset in the quantized flux through the ring. In our experiments the π-phase-shift is the result of the changing sign of the order parameter wave function between the s- and $d_{x^2-y^2}$-wave in niobium and YBCO respectively.

The flux Φ in the superconducting loop can be generated in two ways: the self-generated flux and the externally applied magnetic flux, so by (2.23)

$$I_s L + \Phi_e = \left(\mathrm{n} + \frac{1}{2}\right)\Phi_0, \mathrm{n}\epsilon\mathbb{Z} \tag{2.24}$$

where L is the self-inductance of the loop and Φ_e is the flux applied by an external magnetic field.

2.4. Scanning superconducting quantum interference device microscopy

2.4.1 SQUIDs

The measurement device used in this thesis is called a SQUID, which is short for Superconducting Quantum Interference Device. The SQUID is the most sensitive measurement device for magnetic flux and can do non-destructive measurements. For these reasons, SQUIDs have applications in several fields like geology, medicine and astronomy [15, 16]. The scanning SQUID microscope (SSM) is able to measure the flux through an area of several hundreds of micrometers per side. A description of the type of SQUID used during the research conducted for this thesis is given in [17].

2.4.2 Working principle

The SQUID sensor is a superconducting loop. As shown in equations (2.13) and (2.23), the flux through this loop is quantized. As a result of this quantization, any magnetic field penetrating the loop will be compensated for by a current circulating around the loop. When the magnetic field becomes too strong, the sign of the current will change to induce a magnetic field in the loop that rounds the magnetic flux penetrating the loop to the next integer multiple of the magnetic flux quantum Φ_0. The current that is now flowing through the loop is a measure for the magnetic field that is externally applied to the loop. This external magnetic field can, for example, be the earth's magnetic field or the magnetic field coming from a sample.

2.4.3 Conversion of SQUID measurement data to flux

In the following, the method used to integrate the flux from the SSM images is explained. Each image consists of a set of pixels, which have an x-, y- and associated N-value (which is converted to a color scale), see figure 2.4(a). N is proportional to Φ_s, the flux detected by the sensor pick-up loop for that particular pixel. To integrate the flux, first the values N are summed for all pixels within a radius r from the center of the ring. The integration area is given by the sum of all pixels times the area per pixel A_p. In figure 2.4(b), $\sum N$ is plotted as a function of the integration area (black solid points). In the absence of a background magnetic field $\sum N$ should increase with r until r reaches the inner radius of the ring, and then remain constant until the outer diameter is reached. To compensate for constant offsets in the SQUID signal $\sum N$ is fitted to a straight line between an inner radius R_{in} and an outer radius R_{out}, see figure 2.4(a) and the blue line in figure 2.4(b). R_{in} and R_{out} are chosen well within the superconducting material. In figure 2.4(b) the resulting $\sum N^*$ after background subtraction is shown (red solid points).

There is a difference between the area of the sensor pick-up loop A_s and the pixel area A_p. The flux through one pixel on the sample equals

$$\Phi_p = BA_p \tag{2.25}$$

The flux through the sensor pick-up loop is given by

$$\Phi_s = BA_s \tag{2.26}$$

where A_s is the effective area of the sensor pick-up loop which is calculated to be 24.6 μm^2 at 4.2 K. This effective area is comparable to the actual area of the pick-up loop, but the magnetic field that is pushed through the loop as a result of the Meissner effect is incorporated which makes the effective area slightly bigger than the actual area. This effect is called flux focusing. The effective area of the pick-up loop is found by calibrating it with a single vortex. A single vortex always has a trapped magnetic flux of $1\Phi_0$. By calculating the magnetic flux of this vortex, some amount of flux is found. Assuming the initially assumed effective area is not perfectly right, this amount of flux will not equal exactly $1\Phi_0$. A look at equation (2.28), which will be explained later on in this section, shows that multiplying the initially assumed sensor pick-up loop area by the measured amount of flux quanta Φ_0 will yield the right effective area A_s of the sensor pick-up loop.

When comparing equation (2.25) with (2.26) it can be seen that the magnetic field is assumed to be constant throughout the complete loop and throughout the sample. This is justified by assuming that both the sensor and the ring are small enough to say that fluctuations in magnetic field are minimal. The desired quantity that is measured is the flux through a pixel on the sample surface, so it is necessary to find an expression for this in terms of the measured flux through the pick-up loop Φ_s. This expression can be found by substituting equation (2.26) into equation (2.25). The result of this substitution is

$$\Phi_p = \Phi_s \frac{A_p}{A_s} \tag{2.27}$$

The flux through a ring is equal to the summation of Φ_p over all pixels within the inner radius of the ring. Each pixel has an area A_p of 6 × 6 μm^2 (or 3 × 3 μm^2 in other SSM images), which is determined by the scan step size (6 μm or 3 μm for the experiments conducted in this thesis). However, N^* is related to the flux through the pick-up loop of the sensor Φ_s, with a different area A_s of 24.6 μm^2, which should be taken into account when integrating the flux. In general, the flux Φ_p through a pixel is related to the flux through the sensor pick-up loop Φ_s via (2.27). The value N is determined from the flux Φ_s through the SQUID pick-up loop via the flux-to-voltage transfer Φ-to-V of the flux-locked loop, the gain and an analog-to-digital conversion step (16 bits for ±10 V). Combining this with equation (2.27) we find the following relation between $\sum \Phi_p$ and $\sum N^*$

$$\sum_{r<R_{in}} \Phi_p = \frac{1}{\Phi-\mathrm{to}-\mathrm{V}\cdot\mathrm{gain}\cdot\left(\frac{2^{16}}{20}\right)} \frac{A_p}{A_s} \sum_{r<R_{in}} N(r)^* \tag{2.28}$$

Inserting the values for the flux-to-voltage transfer (14-18 V/Φ_0) and gain (1-2 ×), the integrated flux $\sum \Phi_p$ can be directly calculated as a function of the integration area. The result is shown in figure 2.4(c). Φ_{ring} can be evaluated at any value of r between R_{in} and R_{out}, as by construction it is constant within experimental noise between these values.

Throughout this section, the distance from the sensor pick-up loop to the sample is not taken in as a factor between the measured signal and the calculated flux. A justification for this is given at the end of section 3.2.2.

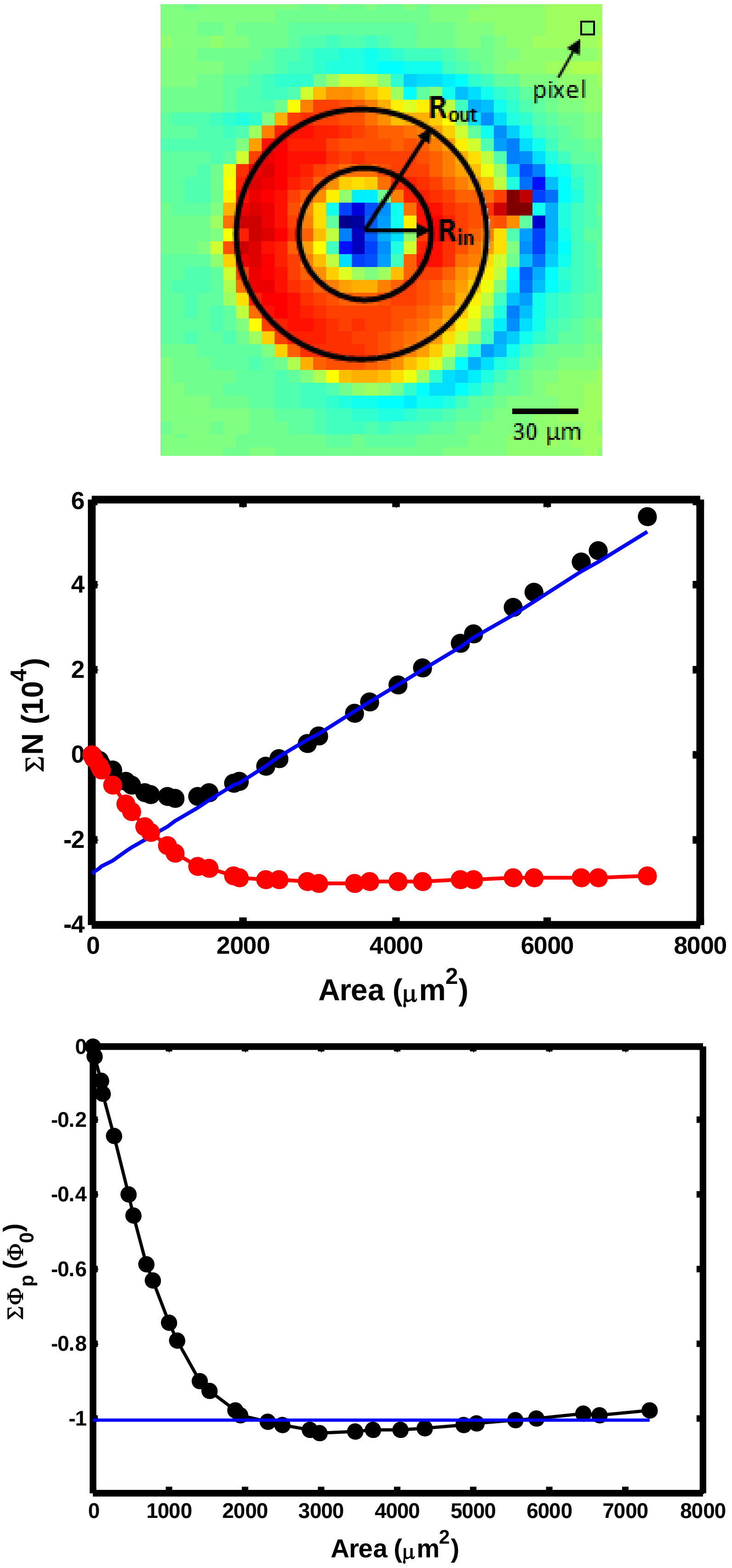

(a)

(b)

(c)

Figure 2.4: (a) SSM image for the 0-ring with θ_2 = 332° (integer magnetic flux quantization), showing the size of a pixel and the inner- and outer radii used for background subtraction. (b) Integrated N as a function of integration area. Black solid points: $\sum N$, blue line: fit between R_{in} and R_{out} , red solid points: $\sum N^*$. (c) Integrated flux $\sum \Phi_p$ as a function of integration area.

2.5 Mapping of current in a sample

Given a measurement of a magnetic field's z-component through a sample, it is possible to create a mapping of the current density in the sample. This mapping can be used to find out if a superconducting sample is in its superconducting state or if the superconductivity in the sample is in some way destroyed. This destruction can be the result of high currents flowing in the sample or temperatures above the critical temperature.

There are complications on creating this mapping. Maxwell's equations are all only useful for more-dimensional fields because of the use of the curl and divergence operator. In this project, only the z-component of the magnetic field is known. For this reason it is impossible to use Maxwell's equations when calculating the current. The Biot-Savart law

$$\mathbf{B} = \frac{\mu_0}{4\pi}\int \frac{\mathbf{J}(\mathbf{r}') \times (\mathbf{r} - \mathbf{r}')}{|\mathbf{r} - \mathbf{r}'|^3} d^3\mathrm{r}' \tag{2.29}$$

can be used if some assumptions are made.

When looking in Cartesian coordinates, the Biot-Savart law implies that each component of the induced magnetic field is generated by the two orthogonal components of the current density field. The information that is known is only B_z, which contains information on two components of the current density field, J_x and J_y. To compute this problem, we will have to assume that $J_z = 0$. In general this is not necessarily true, but if samples are sufficiently small, the approximation can be made. With this assumption done, the integral in equation (2.29) in Cartesian coordinates can be computed for the z-component.

The assumption is made that there is no current loss and that no current is created, so $\nabla \cdot \mathbf{J} = 0$. The simplified integral that is now left can be computed by using Fourier transformation. Using the integral property of the Fourier transform, where integration in real space corresponds to multiplying by a frequency term in Fourier space, this integral can be computed. The result is a direct relation between the Fourier transforms of J_x and J_y. These are now scaled with respect to each other, where the scaling is the ratio between the frequency terms picked up by using the Fourier transform's integration property. The x- and y-component of the current density can now be found by computing the inverse Fourier transform. A measure for the total current is found by adding the resulting $J_x\hat{\mathbf{x}}$ and $J_y\hat{\mathbf{y}}$ using vector addition.

Fourier transforming gives rise to a few problems when solving the integral. The Fourier transform implicitly assumes periodicity. This results in some artifacts on the sides of the mapping. These artifacts are shown as lines that are not closed and can therefore be identified on the picture. Another problem resulting from the Fourier transform comes from filtering the values. High frequency values can be the result of a background signal and are therefore filtered out by using a Hanning window. The removing of high frequency signals gives a blurring effect on sharp edges. This means a loss in resolution. A more detailed mathematical justification of the program is found in [18].

From the program's result, measures can be found for J_x, J_y and $|\mathbf{J}|$. J_x and J_y can be used to deduce the direction of the current. $|\mathbf{J}|$ is used to see where the current is strong or weak, but does not contain information about the actual direction of the current.

Chapter 3. Experimental aspects

3.1. Introduction

In this chapter the setup that is used in the experiment is discussed. First, the SQUID sensor will be explained. The SQUID sensor is the part of the setup that measures the magnetic flux through the sample. There will be an overview of the basic working of the sensor and the electronics behind it. In the second part, there is an explanation on some external devices used in the setup. These devices include, among others, an amplifier to enhance the signal and a solenoid with a current source to alter the magnetic field on the setup. Lastly, there is a description of the fabrication of the sample and the possible influences this process has on the performed measurements.

3.2. The holder

The SQUID sensor is attached to a holder. This holder contains not only the sensor, but also a cantilever to ensure the right positioning of the SQUID and electronics. The sensor should be mounted on the cantilever as shown in figure 3.3, this way ensuring that the pick-up loop of the SQUID is always as close to the sample as possible. If the pick-up loop is close to the sample, the measured signal will be strongest. However, if the loop touches the sample, the loop can be polished away and might even damage the sample.

If the sensor comes in contact with the sample, the cantilever will bend and the contact angle between the sensor and the sample will decrease to 10°. As long as the sensor and the sample are not in contact, the cantilever will not bend. In this case the angle between the cantilever and the sample will be 30°.

The holder has to be mounted into the setup. For practical reasons, it is important to align the cantilever and the sample with either the x- or y-axis of the motor. This way, positioning the sample above the sensor will be easier. When this is done, it is possible to change the position of the SQUID sensor with respect to the sample. However, due to the difference between room temperature and the operating temperature (the boiling point of helium at 4.2 K), the cantilever will bend due to thermal expansion and the position of the sensor will change. This thermal expansion only has a relevant effect in the direction that the cantilever is pointing, so either the x- or y-coordinate on the scanned sample will not change.

3.2.1 The SQUID sensor

The sensor is an open, superconducting loop with two Josephson junctions. The basic working of the SQUID sensor is explained in section 2.4.2. Before the sensor is used it has to be cut in such a way that the pick-up loop can get as close to the sample as possible. Pictures of a cut and an uncut sensor are taken using an optical microscope. These are shown in figure 3.1.

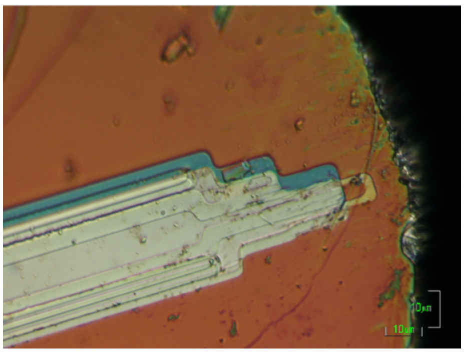

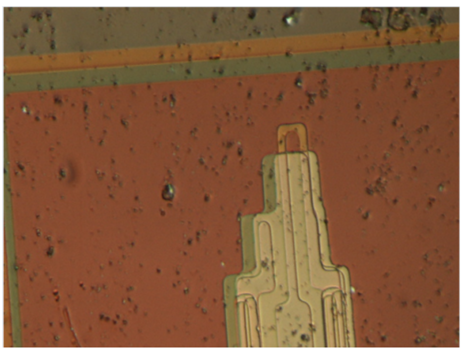

Figure 3.1: In the above figures, a cut (left) and an uncut SQUID sensor (right) are shown. The photos are taken under an optical microscope. From these pictures, characteristic lengths of the sensor can be measured.

Figure 3.2 shows a schematic representation of the sensor pick-up loop with the characteristic lengths indicated in the picture.

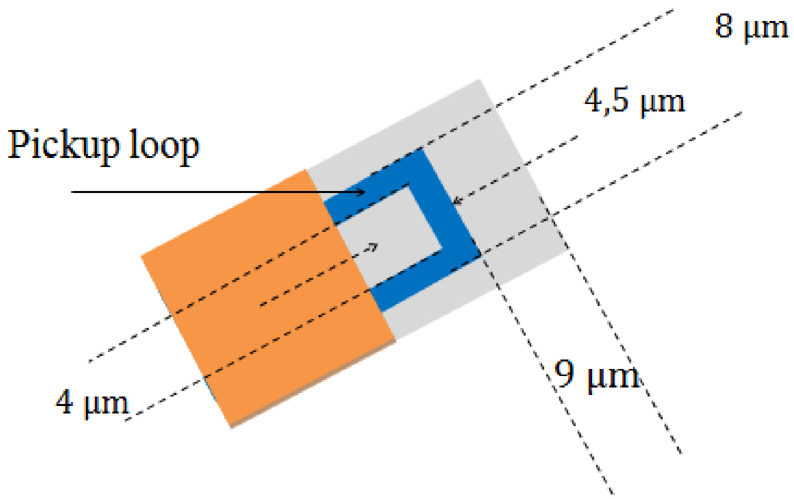

Figure 3.2: This figure shows a schematic representation of the SQUID sensor. The shape of the sensor pick-up loop is roughly equal to a rectangle, as can be seen in figure 3.2. The interior of the rectangle has dimensions of approximately 6 by 4 µm. The thickness of the pick-up loop edge is 2 µm. The ideal distance between the edge of the sensor and the edge of the pick-up loop is a bit more than the length of the loop. In this case this distance is 9 µm.

3.2.2 Distance to the sample

The distance to the sample has to be set accurately. Being close to the sample ensures a greater sensitivity but also increases the chance of colliding with the sample. If the sensor and the sample collide, this might damage both the sensor and the sample. If the very edge of the sensor is touched by the sample, the setup is in so called *contact mode*. To approach the sensor with the sample, the sample can directly be moved towards the sensor by adjusting the z-position on the motor. It is important to stop the approaching early enough, to be sure not to crash into the sensor. To approach the sample in a more fine manner, the SSM has an approach mode. Pressing the “up”-button on the computer makes the sample go downwards to the sensor in steps. When this is done, an adjustable length is scanned in the x-direction. This process is repeated until a signal is measured from the sample during the scanning. In practice, being far away from the sensor will also introduce a gradient in the signal that is measured. As long as this gradient is present, one can be fairly sure that the sample and sensor are not in contact mode yet.

Because the sensor is positioned at an angle, there is still an effective distance between the sample and the sensor. This distance can be calculated using the geometry of the sensor. The more detailed geometry of the sensor is shown in figures 3.1 and 3.2 in section 3.2.1. The positioning of the sensor with respect to the sample is shown in figure 3.3.

The effective distance between the sensor and the sample depends on the half length of the pick-up loop, on the distance between the end of the sensor and the pick-up loop and on the angle between the sample and the sensor, as shown in figure 3.3. The geometry shows that this distance is equal to $(4.5\ \mu m + 9\ \mu m) \cdot \sin(10°) = 2.3\ \mu m$ in contact mode. Here, 4.5 µm comes from the half length of the pick-up loop and 9 µm comes from the distance between the pick-up loop and the edge of the sensor. The angle between the sample and the pick-up loop in contact mode is 10°. The distance of 9 µm between the pick-up loop and the edge of the sensor is only a typical value that can deviate for different sensors. This distance is only determined by how the sensor is cut.

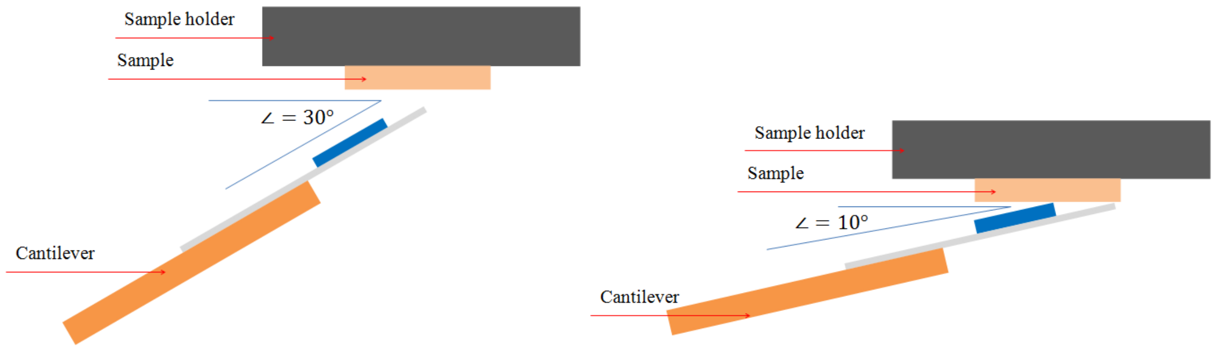

Figure 3.3: The left figure shows a schematic of the SQUID sensor in non-contact mode with the sample. The typical angle between the sensor and the sample for this mode is 30°. When the sensor comes in contact with the sample, the SQUID sensor is in contact mode, shown in the right figure. The typical angle between the sensor and the sample in contact mode is 10°.

Even though the distance to the sample plays a role in the sensitivity of the measurements, it is important to note that it is not necessary to correct for this distance when analyzing a measurement, as long as the distance remains constant. Intuitively, one might think that the distance to the sample has an influence on the measured flux. This is a result of the flux spreading out in space after passing through the ring on the sample. This way it looks like the flux can only be accurately measured by holding the pick-up loop precisely on the ring. However, when an area is scanned that is larger than the ring, the flux that diverges away from right above the ring will also be scanned at some point. This does mean the measurement does not exactly yield the flux profile on the sample, but it actually shows the flux profile at a distance from the sample. Integration of this flux profile yields the same amount of flux through the superconducting ring, but it does not yield an accurate picture showing where the flux comes from.

3.3. External devices

There are a number of external devices used in the SSM setup. They are used for various reasons, such as introducing a magnetic field to the sample or enhancing the measured signal. One of these components is a solenoid. The solenoid can be attached to the setup in such a way that both the SQUID sensor and the sample are inside the solenoid. If a current is now running through the solenoid a magnetic field is induced. The magnetic field that is induced is generally a function of the location inside the solenoid, but it can be assumed constant when the sensor and sample are kept in the center. This is justified by noting that in the center of the solenoid, a change in location has only a small effect on the magnetic field, as is shown in figure 3.4.

The magnetic field applied on the sample is offset by the earth's magnetic field. The earth's magnetic field can be compensated for using the field induced by the solenoid. Previous measurements have shown that the earth's magnetic field is compensated for when a current $I = -0.65$ mA runs through the solenoid. This corresponds to a magnetic field in the z-direction of $B_z = 42$ mG/mA $\cdot$ 0.65 mA $= 27.3$ mG. Here, the factor 42 comes from the calibration graph in figure 3.4.

An amplifier is also incorporated into the system. The amplifier introduces a gain between 1 and 100. The main reason for using this amplifier is that the signal directly coming from the scanning SQUID is too small to measure it accurately.

During most measurements, the amplifier was set to a gain of 1 or 2, dependent on which gave the most practical output. The output as a result of the test signal is measured using a *Tektronix TDS 3012C Digital Oscilloscope*.

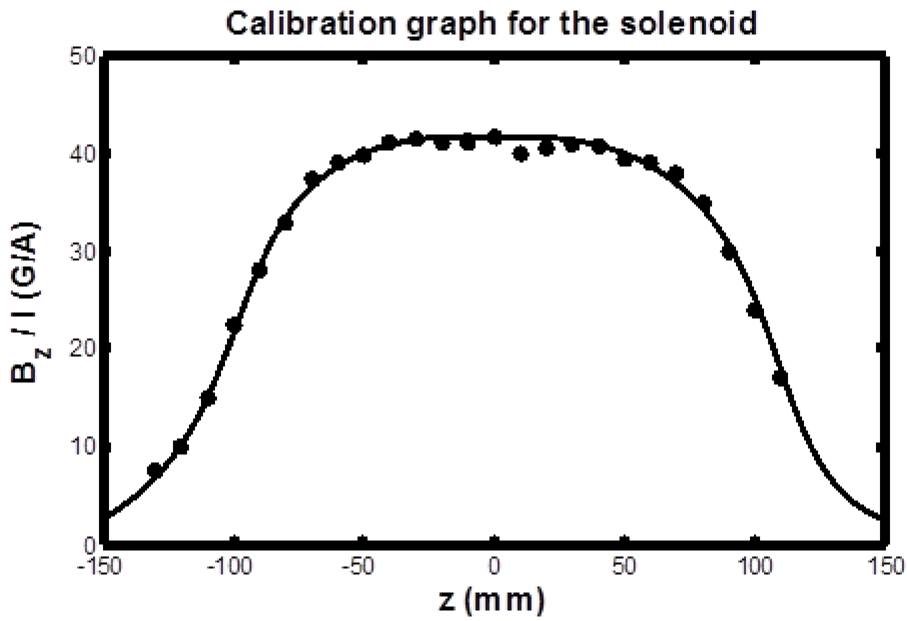

Figure 3.4: Calibration graph for the solenoid used to apply external magnetic fields. The point z = 0 mm corresponds to the the center of the solenoid. An important property of the graph is the small slope of the graph around z = 0 mm. This small slope can be used to minimize the error in the magnetic field. By making sure the sensor and sample are close to the center of the solenoid, the gauss/ampere ratio can be determined with greater precision.

The sample that will be used in this thesis contains niobium. Niobium is a type II, low-T_c superconductor with a critical temperature T_c of 9.2 K. To get to such low temperatures a cryostat is used. The cryostat is filled with liquid helium. The helium level in the cryostat is measured with an *American Magnetics 110*. The device gives a value between 0 and 100 percent. One hundred percent corresponds to a completely filled cryostat. Zero percent however does not correspond to a completely empty cryostat. When the American Magnetics measures a helium level of 0 percent this means that the lowest level the solenoid can get to is reached. For the experiments conducted in this thesis, this effectively means that the amount of helium is not high enough to continue doing measurements when a zero percent helium level is reached.

The position of the sample can be changed with respect to the position of the sensor. A *Newport Universal Motion Controller & Driver* is attached to the system. This motion controller has three components to change the x-, y- and z-position of the sample. When measuring, only the x- and y-controller are used to move the sample across the sensor during a scan. The distance between the sensor and the sample, the z-component, is constant during the scan. The z-controller can be used to approach the sensor before measuring or to retract the sample when the system consisting of the SQUID sensor and the sample is taken out of the cryostat. A schematic overview of the SSM system is shown in figure 3.5(a). A close-up of the scanner is shown in figure 3.5(b). The solenoid that is placed around the scan area during the actual measurements to compensate for stray fields and to apply an external magnetic field in the Dewar, is not shown.

To find the flux-to-voltage transfer Φ-to-V of the flux-locked loop, as mentioned in section 2.4.3, a test function is used. The reaction of the SQUID output to this test function equals the reaction of the SQUID output to the measurement of a magnetic flux equal to one magnetic flux quantum Φ_0. The test function is generated using an *Agilent 33220A 20MHz Function Generator*. When the test signal is turned off, the output can be used to give a measure for the noise level of the measurement. The noise level typically ranges from 30 to 50 mV. However, the noise can significantly increase due to cell phone noise. Cell phones that are turned on in the room where the SQUID measurements are done, will typically give rise to a relatively strong 217 Hz noise.

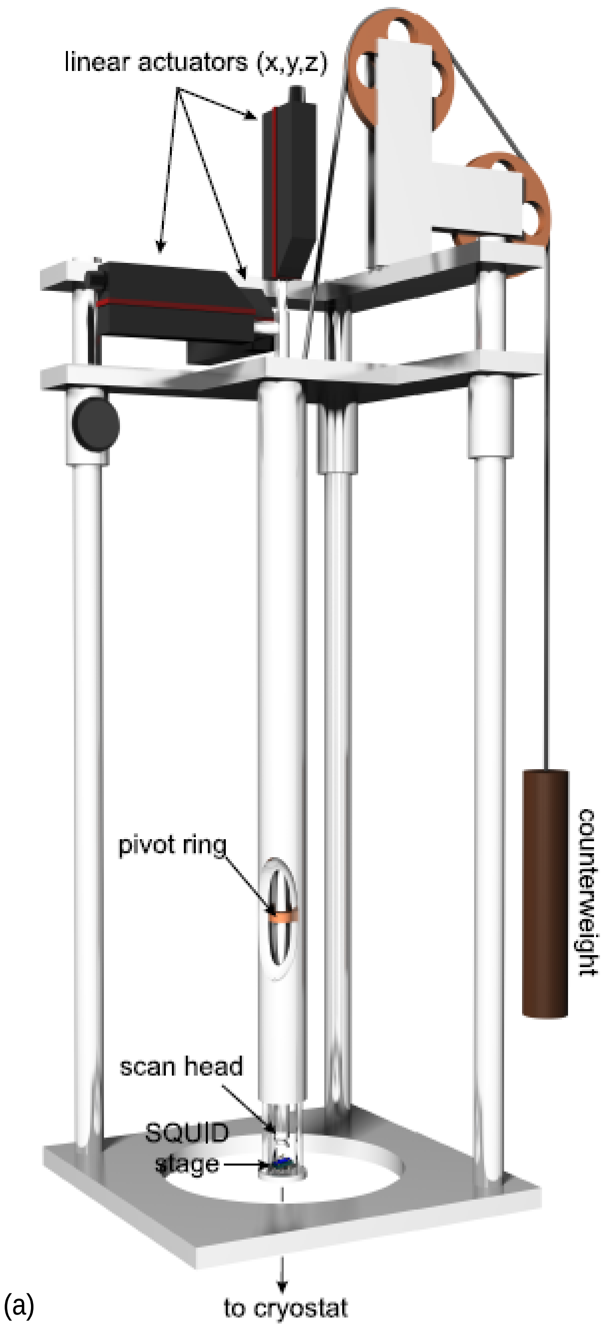

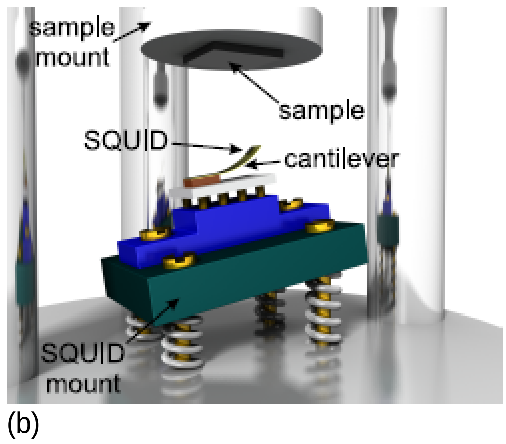

Figure 3.5: (a) Schematic of the scanning SQUID microscope setup. (b) Schematic of the scan head and the SQUID stage (figures adapted from Verwijs [9]).

3.4. The sample

The sample that is used in the measurements done as a part of this project, was created and used several years ago by dr. C.J.M. Verwijs as a part of his research done in[9]. The sample is already more than five years old, so the quality may have been degraded as years passed. Most parts in section 3.4 were adapted from chapter 4 in [9] written by Verwijs as we did not fabricate the used sample ourselves but used the old sample that Verwijs used.

In this section the general properties of YBCO and niobium will first be discussed. After this the main focus will be on the process of creating the sample.

3.4.1 $YBa_2Cu_3O_{7-\delta}$

Yttrium barium copper oxide (YBCO) exists in several stoichiometric phases, such as $YBa_2Cu_3O_{7-\delta}$ (T_c = 93 K), $YBa_2Cu_4O_8$ (80 K), and $Y_2Ba_4Cu_7O_{14+x}$ (95 K). $YBa_2Cu_3O_{7-\delta}$ is most often used because it is easier to fabricate. In this thesis, YBCO will refer to $YBa_2Cu_3O_{7-\delta}$. The crystal structure of YBCO is shown in figure 3.6(a). The structural and electronic properties of YBCO are strongly dependent on the oxygen deficiency. For $YBa_2Cu_3O_6$ ($\delta = 1$) the crystal structure is tetragonal: the *a*- and *b* crystal axes are equal to each other but different from the *c*-axis. There are four oxygen atoms located in the copper-oxide planes and two atoms are surrounding the two barium atoms. The sites in the *ab*-plane (at the top and bottom of the unit cell in figure 3.6) are empty for $\delta = 1$. When the oxygen content increases, the occupancy of the states in the copper-oxide planes increases and the oxygen divides evenly between sites that are located on the *a*-axis (the O5 sites) and sites that are located on the *b*-axis (the O1 sites). When $7 - \delta$ reaches a value of approximately 6.35 a phase transition occurs. The YBCO goes from the non-superconducting tetragonal phase to the superconducting orthorhombic phase. For the orthorhombic crystal structure the *a*-, *b*- and *c* axes differ from each other. When the oxygen content $7 - \delta$ is increased even further the occupancy of the O1 sites increases but the occupancy of the O5 sites starts to decrease, as indicated in figure 3.6(b). The cell constants and critical temperature of YBCO depend strongly on the oxygen deficiency. Experiments provided evidence for a maximum T_c around $\delta = 0.13$. All YBCO thin films that are used in this thesis are close to optimal doping, resulting in a critical temperature of approximately 92 K and cell constants $a = 3.82$ Å, $b = 3.89$ Å, and $c = 11.65$ Å.

Superconductivity in YBCO is believed to take place in the copper-oxygen planes. These planes are not perfectly flat but are slightly bend towards the Y^{3+}-ion. Despite this bending, superconductivity can still be regarded as a 2-dimensional phenomenon. Because of this it is very important that YBCO thin films are grown epitaxially. The devices described in this thesis contain *c*-axis oriented YBCO films that were epitaxially grown on $SrTiO_3$ substrates. $SrTiO_3$ has a simple cubic crystal structure, and its lattice constant of 3.905 Å matches well with the *a*- and *b* axes of YBCO.

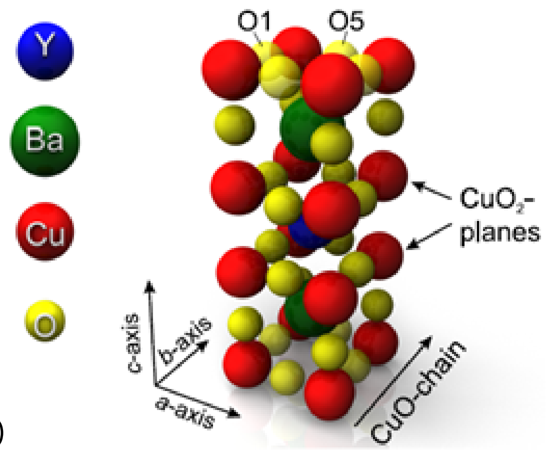

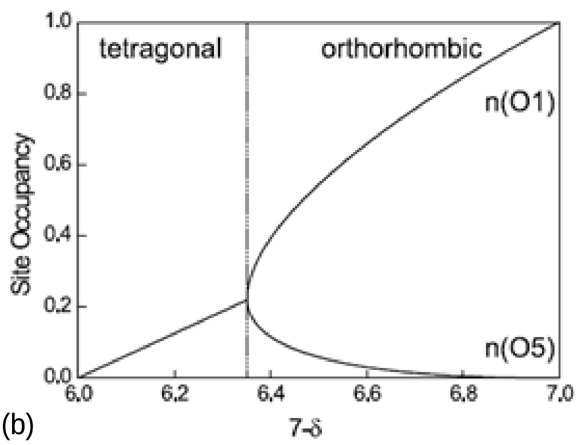

Figure 3.6: (a) Schematic representation of the unit cell of $YBa_2Cu_3O_{7-\delta}$. The oxygen sites at the top and (equivalently) bottom of the unit cell, indicated with a slight transparency, can be separated in two pairs: the O1 sites are located on the *b*-axis and the O5 sites are located on the *a*-axis. (b) Occupancy of the O1 and O5 sites as a function of the oxygen content $7 - \delta$ (figure adapted from Verwijs [9]).

3.4.2 Niobium

In this thesis, niobium is used as a low-T_c superconductor. Niobium is the only elemental superconductor that is type II. The reason why this element is chosen instead of other low-T_c superconductors is its relatively high critical temperature of 9.25 K. Because of this high critical temperature it is possible to cool the sample using liquid helium, which has its boiling point at 4.2 K. Niobium oxidizes easily to a variety of oxides and in this way it is capped by a thin Nb_2O_5 layer, which prevents further oxidation. This natural Nb_2O_5 coating is dense, mechanically hard and stable. The melting point above 2000 K and low diffusivity below 400 K result in long time stability and robustness to thermal cycling. All these factors combined make niobium one of the most popular metallic superconductors. The crystal structure of niobium is BCC. The niobium films that were used in our experiments consist of polycrystalline niobium (grain size ≈ 60-80 nm) which is much easier to fabricate than the epitaxially grown YBCO. The high chance of oxidation of niobium poses a problem at the Josephson contacts between YBCO and niobium. When brought into contact with YBCO, the niobium can oxidize using the oxygen in the YBCO. To prevent this oxidation, a thin layer of Au is deposited between the electrodes. The gold layer is chemically inert and will therefore reduce the oxidation at the junction.

3.4.3 Ramp-type Josephson junctions

The YBCO/Nb rings are connected via Josephson junctions. These connections require special attention because of the nature of superconductivity in YBCO. As mentioned, the superconductivity in YBCO is believed to take place in the copper-oxygen planes. Because of the suppressed gap in the *c*-axis direction, planar junctions are not suitable to connect the YBCO electrode to the *s*-wave niobium electrode. Studies to Josephson contacts between high-T_c and low-T_c superconductors revealed that ramp-type Josephson junctions can be used to fabricate reliable junctions.

The cross section of a ramp-type Josephson junction is shown in figure 3.7, where the YBCO film is grown with the CuO_2 planes parallel to the substrate. For this geometry, the *ab*-plane of the YBCO base electrode is aligned with the niobium top electrode. Because of the YBCO *d*-wave symmetry the coupling will be the largest when the junction edge is aligned with the *a*- or *b*-axis of the YBCO crystal structure.

The overlap, which is typically a few µm for the sample discussed in this thesis, serves to compensate for small misalignments between the top- and bottom electrodes in the direction of the current. The STO capping layer prevents current in the *c*-axis direction. Therefore the size of the overlap will not have an influence on the junction critical current in this ramp-type geometry. During the design stage, the overlap was always designed such that the niobium overlap has a smaller width (i.e. the out-of-plane direction in figure 3.7) than the YBCO base electrode. This smaller width serves to allow for small in-plane misalignment errors between the top- and bottom electrodes in the direction *perpendicular* to current transport. Without this difference in width, a misalignment would result in the formation of a junction with a π-phase-shift which generates unwanted flux or reduces the critical current of the junction.

Studies on YBCO/Au interfaces show an amorphous layer at the interface between the high-T_c base electrode and the Au layer deposited at the ramp edge. Such an amorphous layer strongly suppresses the critical current density of the Josephson junction. For this reason a restoring interlayer is deposited and annealed *in situ* prior to the deposition of the gold barrier. This interlayer, with a typical thickness of 7 nm, restores the surface and leads to clean, reproducible and well-defined interfaces.

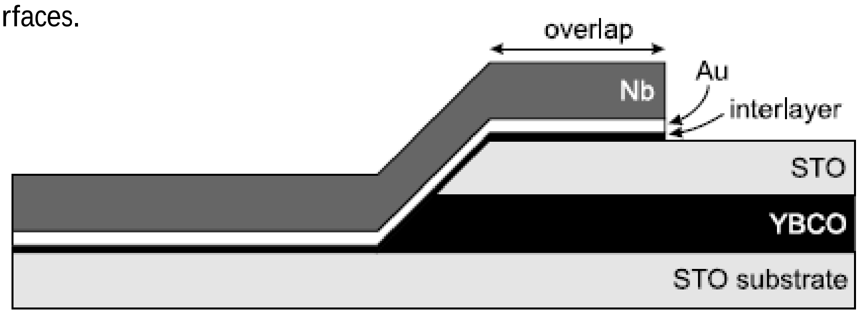

Figure 3.7: Schematic cross section of a ramp-type Josephson junction connecting the high-T_c superconductor YBCO to the low-T_c superconductor niobium (figure adapted from Verwijs [9]).

3.4.4 Fabrication procedure

This section is concerned with the practical realization of the YBCO/Nb ramp-type Josephson junctions. The general fabrication procedure will be outlined.

The fabrication procedure is schematically illustrated in figure 3.8. After cleaning and a surface cleaning step, a [001]-oriented YBCO film is epitaxially grown on the STO substrate using pulsed laser deposition (PLD). During the same fabrication step an STO layer is deposited on top of the YBCO film. Then a layer of resist is spun on the sample in which the shape of the base electrode is patterned using optical lithography. Next the parts of the bilayer that are not covered by resist are etched away using argon ion milling. To ensure a well-defined ramp for all junction angles, the sample is rotated during etching and oriented at an angle of 45° with respect to the argon ion beam. After the resist is removed, a thin (~7 nm) YBCO layer is grown (again using PLD) and annealed in order to restore the ramp which has been damaged during the argon ion milling process. After this restoration step the gold barrier is applied *in situ*, also using PLD. On top of the gold layer a resist layer is spun in which the shape of the counter electrode is defined using optical lithography. In the final deposition step niobium is sputtered onto the sample. Lift-off is used to remove the resist and unwanted niobium. In the last step, the redundant uncovered YBCO/Au layer is removed by argon ion milling. Several processing steps are discussed in more detail in [9].

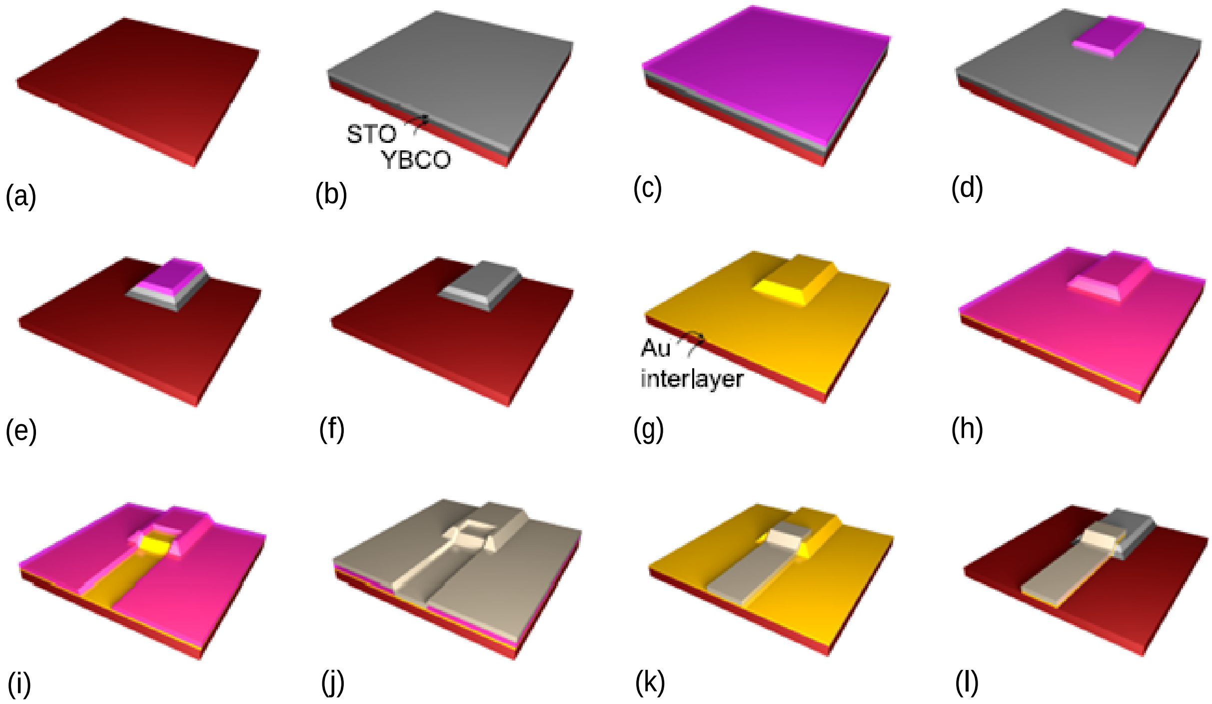

Figure 3.8: Processing steps for the fabrication of YBCO/Nb ramp-type Josephson junctions. (a) Treated STO substrate. (b) Pulsed laser deposition of the YBCO-STO bilayer. (c) Application of photoresist. (d) Patterning of photoresist. (e) Argon ion milling. (f) Resist removal. (g) Pulsed laser deposition of the YBCO interlayer and gold barrier. (h) Application of photoresist. (i) Patterning of photoresist. (j) Sputter-deposition of niobium. (k) Lift-off. (l) Removal of redundant Au and YBCO (figure adapted from Verwijs [9]).

3.5 Experiments on a 0- and a π-ring

The layout of the rings that are used is depicted in figures 3.9(a)-(c). The ring connects a YBCO base electrode to a niobium counter electrode via two ramp-type Josephson junctions. Depending on the geometry such a ring can be either a 0-ring which contains a flux $n\Phi_0$, or a π-ring which contains a flux $\left(n + \frac{1}{2}\right)\Phi_0$ provided the ring is in the so-called *large inductance limit*, i.e. $LI_c \sim \Phi_0$. This is shown in figures 3.9(d)-(f). For a predominantly *d*-wave symmetry the rings (d) and (f) will be a 0- and π-ring, respectively, but the behavior around the nodal directions depend critically on the details of the order parameter symmetry. For a pure *d*-wave superconductor the transition from a 0- to π-ring occurs at an angle of 45 degrees. An *s*-wave admixture would result in a shift of the 0- to π-transition [9]. For the two different rings used in this thesis the Josephson junction angle is far away from the nodal angles and thus YBCO can be considered as a pure *d*-wave superconductor.

An array of 72 rings was fabricated with one junction kept at a constant angle (-22.5 degrees) and the second junction angle varying in intervals of 5 degrees. The rings were fabricated using the procedure described in section 3.4. The YBCO-STO bilayer has a thickness of 340 nm (YBCO) + 70 nm (STO). The choice for a rather thick YBCO layer was made to enhance the critical current. The critical current of the junctions along the nodal directions will be strongly suppressed. A thick YBCO layer will result in larger critical currents and therefore helps to stay in the large inductance regime, which is crucial for our experiments. The thickness of the gold is 16 nm and the niobium counter electrode has a thickness of 160 nm. The YBCO semi-rings have an inner radius of 15 µm and an outer radius of 65 µm, the niobium rings have an inner radius of 20 µm and an outer radius of 60 µm. The YBCO semi-rings were chosen wider than the niobium semi-rings to ensure a single straight junction: a corner in the YBCO under the niobium overlap results in a corner junction, which in turn can result in a spontaneously generated current. The 72 rings are spaced by 400 µm in a square array. In chapter 5 in [9], Verwijs proves that the rings are indeed in the large inductance limit.

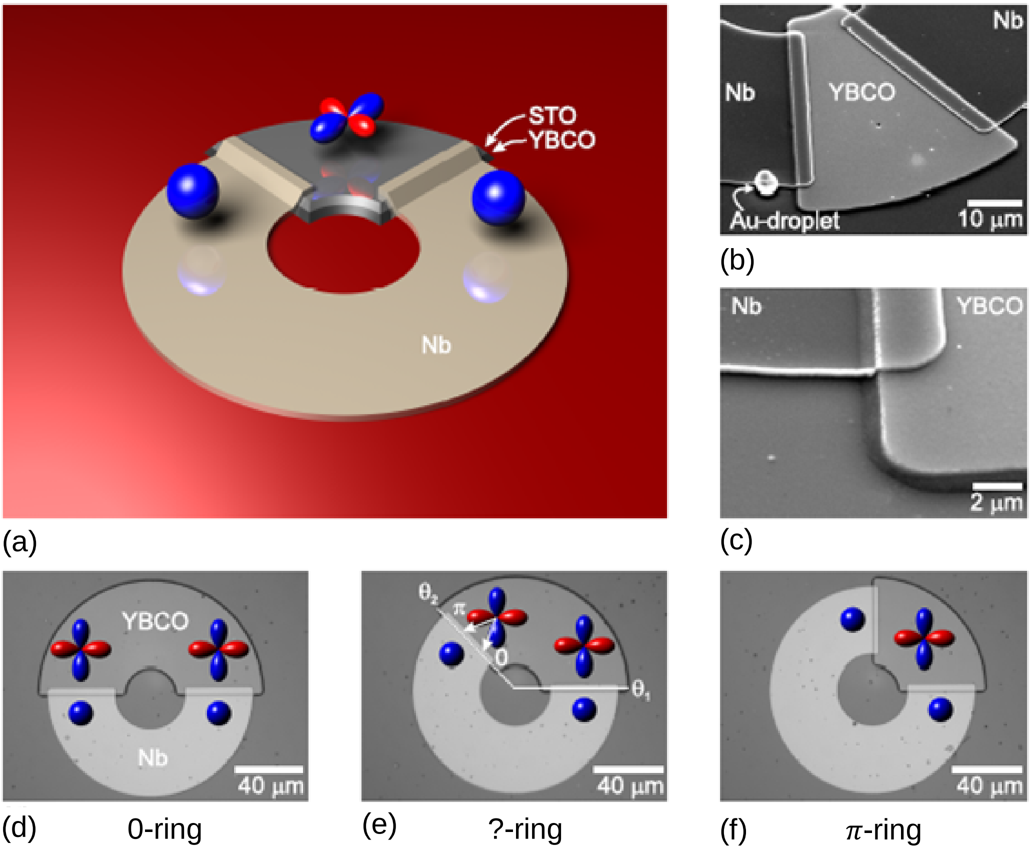

Figure 3.9: (a) Schematic of the YBCO/Nb rings used in the experiment. (b) Scanning electron microscopy (SEM) picture of the YBCO 'island' which is contacted by the niobium counter electrode via two Josephson junctions. (c) SEM picture of the ramp-type junction between YBCO and niobium. (d)-(f) Optical micrographs of superconducting YBCO/Nb rings in three different geometries. The angle of the first junction is fixed at an angle θ_1 = 0°. By tuning the angle θ_2 of the second junction the ring can be (d) a 0-ring, (e) a ring that can either be a 0- or a π-ring, depending on the details of the YBCO gap symmetry, or (f) a π-ring (figure adapted from Verwijs [9]).

The 0- and π-ring on which the measurements are done in the experiments in this thesis are indicated in both figure 3.10 (schematic overview) and figure 3.11 (optical micrograph).

As can be seen in the schematic overview the π-ring is the upper ring in the indicated area and the π-ring's YBCO part ranges from the constant $\theta_1 = -22.5°$ to the variable $\theta_2 = 272°$; the 0-ring is the lower ring in the indicated area and the 0-ring's YBCO part ranges from $\theta_1 = -22.5°$ to $\theta_2 = 332°$.

The angle through which YBCO occurs is $\theta_\pi = -\theta_1 + \theta_2 = 294.5°$ for our π-ring and $\theta_0 = 354.5°$ for our 0-ring. Because YBCO is assumed to be a pure *d*-wave superconductor, the transitions from a 0-ring to a π-ring occur at the angles: $\theta = 45°; 225°$. And the transitions from a π -ring to a 0-ring occur at the angles: $\theta = 135°; 315°$. So indeed, we are dealing with a 0-ring ($\theta_0 = 354.5° > 315°$) and a π-ring ($\theta_\pi = 294.5° < 315°$).

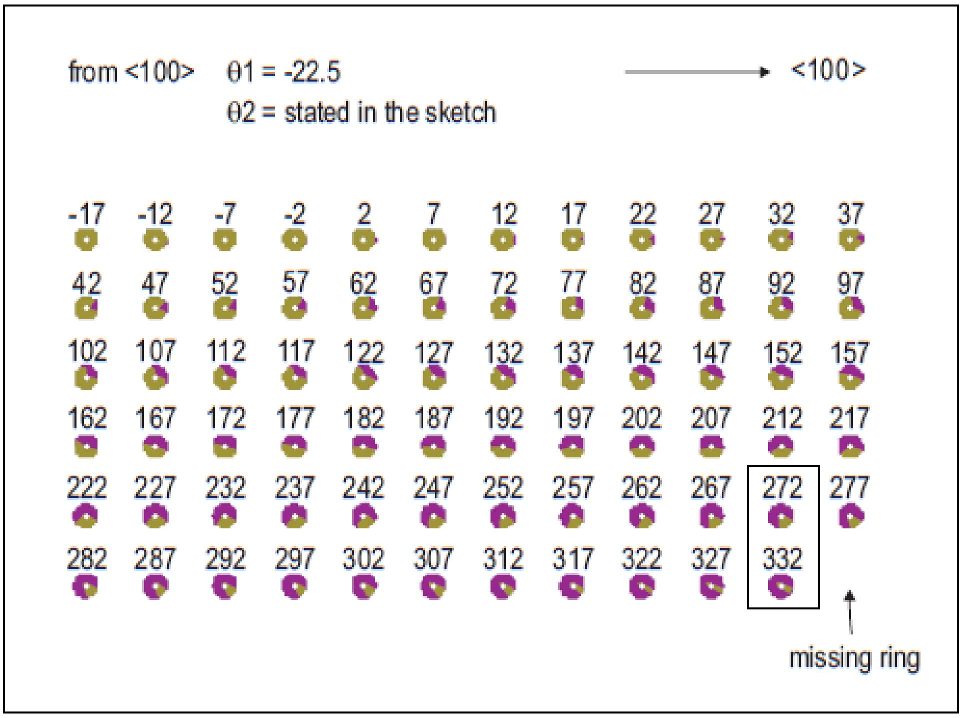

Figure 3.10: Schematic overview of the entire sample and the two rings used in the experiments. Courtesy of Ariando [19]. The small black rectangle shows the 0-ring and π-ring on which the measurements are done in this thesis.

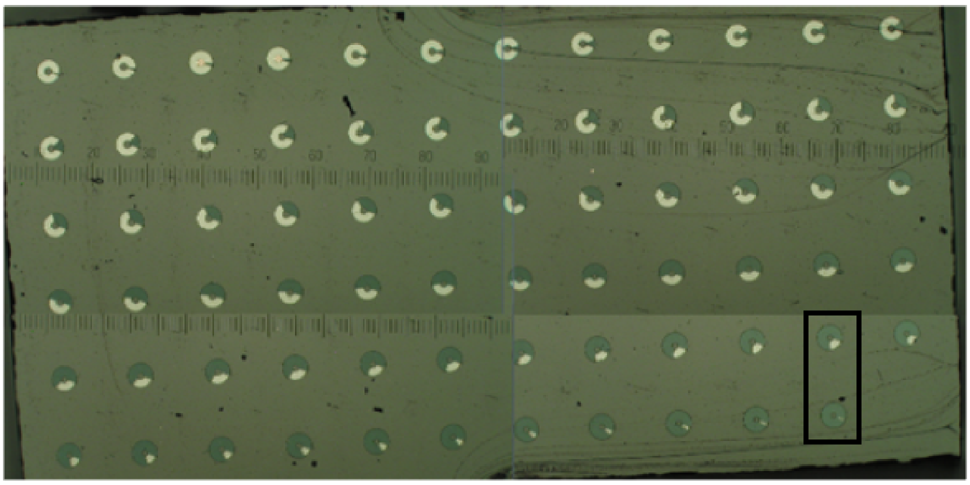

Figure 3.11: Optical micrograph of the entire sample and the two rings used in the experiments. The black rectangle shows the 0-ring and π-ring on which the measurements are done in this thesis.

3.6 The complete setup

A complete figure of the setup is shown in figure 3.12.

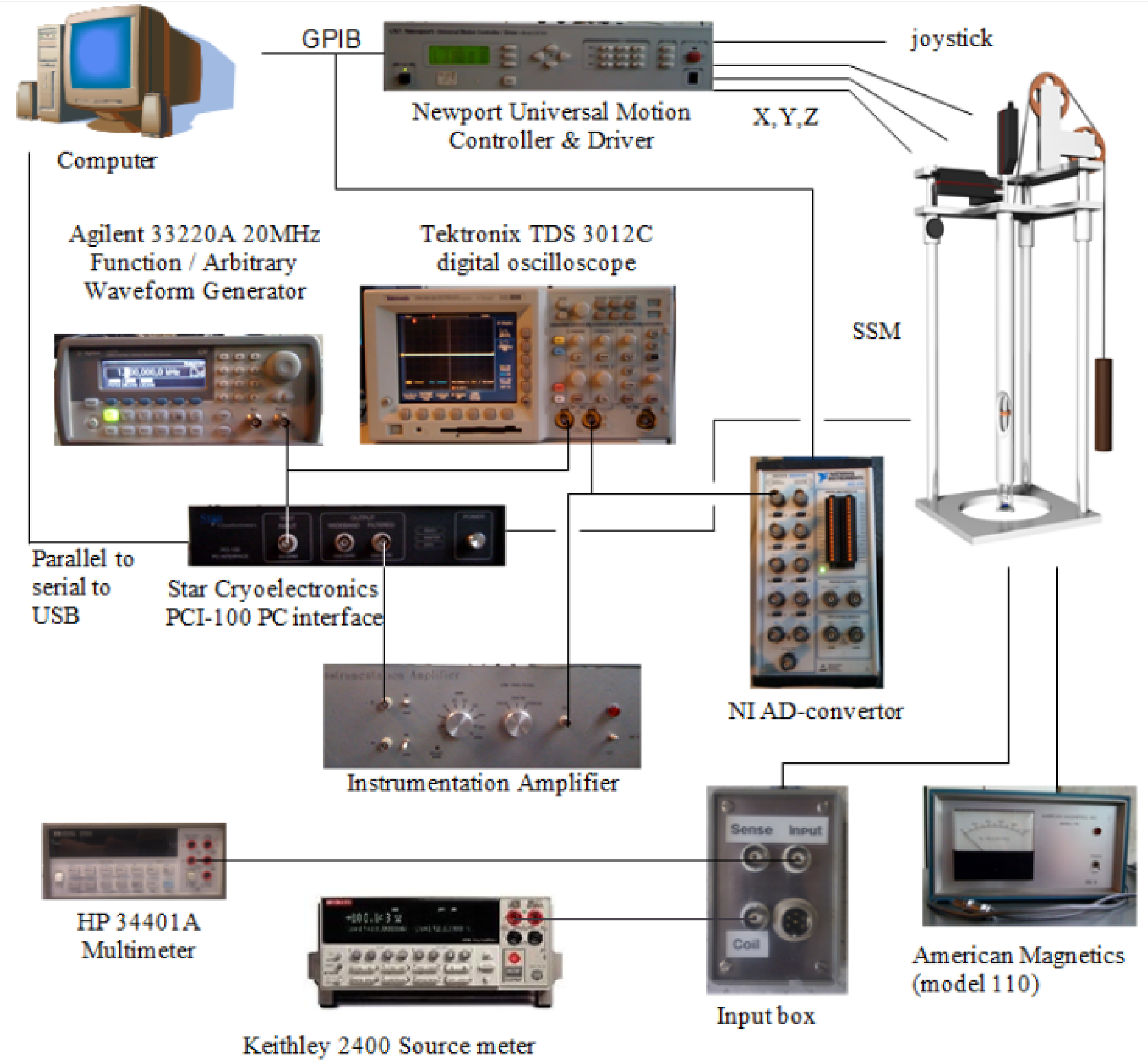

Figure 3.12: This figure shows the complete setup as used in this project. The black lines show how the equipment is linked together (figure adapted from Wijnands [20]).

Chapter 4. Results

4.1. Introduction

This chapter concerns the experimental results. Here, the results will be presented and explained. Two types of measurements are performed. The first set of measurements is performed with the sample cooled in a magnetic field where after the field is set to counter the earth's magnetic field right before the measurement is started. This way, the measurements are done in effectively zero magnetic field. The second set of measurements is also performed with the sample cooled in a magnetic field, but the field strength is not changed before the measurement is started. This way, an external flux is applied on the ring during the measurement.

The discussion and interpretation of the results given in this chapter will mainly be done in chapters 5 and 6.

To calculate the flux through a high-T_c/low-T_c superconducting ring, a MATLAB program based on equation (2.28) and created by dr. C.J.M. Verwijs, is used. The MATLAB scripts making up the program are given in [21].

4.2. Measurements conducted in zero field

After aligning the cantilever with the sample's x-axis, the missing ring on the sample is looked up. When the position of the sensor pick-up loop is close to the missing ring, the missing ring can act as a reference point. With this reference point, it is possible to find out which ring on the sample corresponds to the measured data. Around the missing ring are two especially interesting rings as can be seen in figures 3.10 and 3.11. One with an angle θ_2 = 332°. The other with an angle θ_2 = 272°. Both rings are offset with an angle θ_1 = −22.5°, as mentioned in section 3.5. These two particular rings are expected to show integer flux quantization (0-ring) and a half flux quantum offset (π-ring) respectively.

When the sensor pick-up loop has been positioned close to the missing ring, measurements start with a magnetic field applied on the sample during the cool-down of the scan head and the SQUID stage. This way, magnetic flux gets trapped in the interior of the ring. As soon as the sample has been cooled down and the flux measurement (i.e. scanning the ring on the sample) is running, the current through the solenoid is set to I = 0.65 mA (i.e. B_z = 27.3 mG is applied) as to counter the earth's magnetic field. After the measurement, the system is warmed up above the critical temperature. This process is repeated for several measurements while setting different values for the external applied magnetic field during the cool-down.

The expectation for this measurement series is a number of steps in the flux through the rings. These steps are a result of the spontaneous current in the ring that induces a magnetic field to round the magnetic flux to the closest number of integer or half-integer magnetic flux quanta for a 0- or a π-ring respectively. In the case of the 0-ring with integer flux quantization, the steps are expected to occur at magnetic field strengths corresponding to the following relation:

$$B_\mathrm{n} = \frac{\left(\mathrm{n} + \frac{1}{2}\right)\Phi_0}{A_0}, \mathrm{n} \in \mathbb{Z} \tag{4.1}$$

In the case of the π-ring with half-integer flux quantization, the steps are expected to occur at magnetic field strengths given by:

$$B_\mathrm{n} = \frac{\mathrm{n}\Phi_0}{A_\pi}, \mathrm{n} \in \mathbb{Z} \tag{4.2}$$

The area A in square meter (m^2) of the 0- and π-ring used in equations (4.1) and (4.2) is found by using:

$$A = \frac{\pi}{360}\left(\theta_Y r_Y^2 + \theta_N r_N^2\right) \tag{4.3}$$

Here r_Y and r_N are the inner radii in meter (m) of the YBCO and the Nb semi-rings respectively, θ_Y and θ_N are the angles in degree (°) of the YBCO and Nb parts in the YBCO/Nb ring respectively, and it holds that $\theta_Y + \theta_N = 360°$. For the 0-ring with $r_Y = 15 \cdot 10^{-6}$ m, $r_N = 20 \cdot 10^{-6}$ m, $\theta_Y = 354.5°$ and $\theta_N = 5.5°$, equation (4.3) yields $A_0 = 7.2 \cdot 10^{-10}$ m^2, and for the π-ring with $\theta_Y = 294.5°$ and $\theta_N = 65.5°$, $A_\pi = 8.1 \cdot 10^{-10}$ m^2.

The magnetic field strengths corresponding to the jumps in the expected magnetic flux through the 0- and π-ring are computed using equations (4.1) and (4.2). To be able to use these equations, the area of the ring has to be known. This area is calculated using equation (4.3). Use of these equations gives rise to deviations in the expected magnetic field strengths for which the jumps occur. These deviations are the result of the uncertainties in the area of the 0- and π-ring. Using partial derivatives, the maximum possible deviations in the field strengths can be calculated:

$$\Delta B_\mathrm{n} = \frac{\left(\mathrm{n} + \frac{1}{2}\right)\Phi_0}{A_0^2}\Delta A_0, \mathrm{n} \in \mathbb{Z}, \tag{4.4}$$

$$\Delta B_\mathrm{n} = \frac{\mathrm{n}\Phi_0}{A_\pi^2}\Delta A_\pi, \mathrm{n} \in \mathbb{Z} \tag{4.5}$$

for the respective 0- and π-ring. ΔA_0 and ΔA_π are also calculated using partial derivatives:

$$\Delta A = \frac{\pi}{180}\left(\theta_Y r_Y \Delta r_Y + \theta_N r_N \Delta r_N\right) \tag{4.6}$$

Substituting equation (4.6) in equations (4.4) and (4.5) yields

$$\Delta B_\mathrm{n} = \frac{\left(\mathrm{n} + \frac{1}{2}\right)\pi\Phi_0}{180 A_0^2}\left(\theta_Y r_Y \Delta r_Y + \theta_N r_N \Delta r_N\right), \mathrm{n} \in \mathbb{Z}, \tag{4.7}$$

$$\Delta B_\mathrm{n} = \frac{\mathrm{n}\pi\Phi_0}{180 A_\pi^2}\left(\theta_Y r_Y \Delta r_Y + \theta_N r_N \Delta r_N\right), \mathrm{n} \in \mathbb{Z} \tag{4.8}$$

for the respective 0- and π-ring. Δr_Y and Δr_N are both assumed to be 1 μm. The possible errors $\Delta\theta_Y$ and $\Delta\theta_N$ in θ_Y and θ_N respectively, turn out be negligible and are omitted in the expressions above.

For both the 0- and the π-ring, the location of the jumps in magnetic flux through the ring is predicted. The prediction is done for magnetic field strengths ranging from -60 mG to $+60$ mG and is shown in figure 4.1.

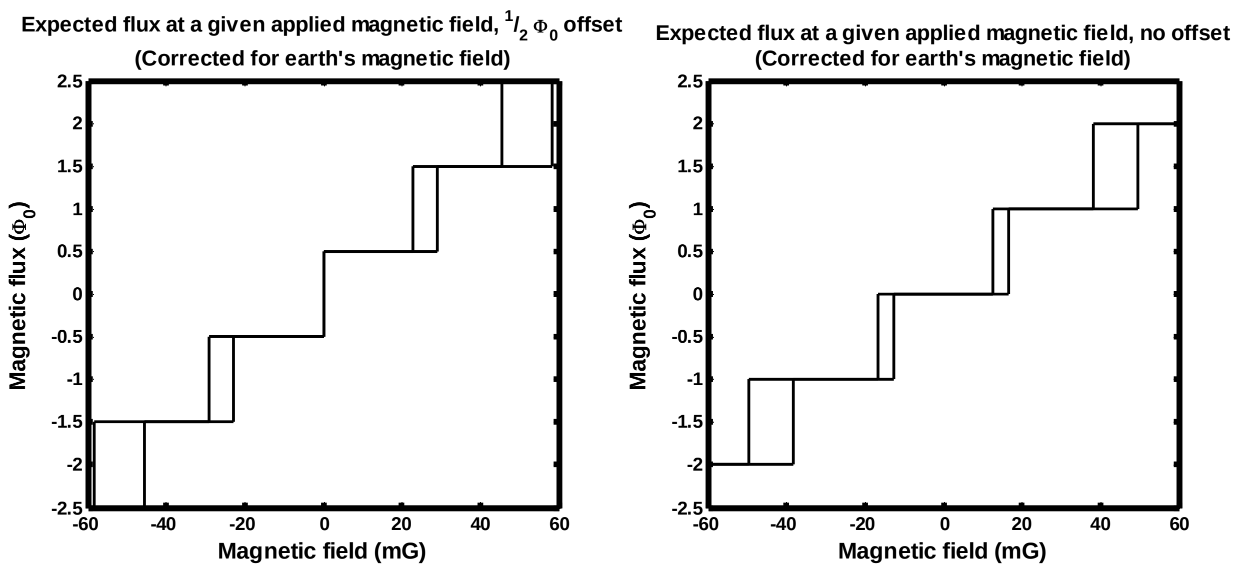

Figure 4.1: (previous page) The left figure shows the expected magnetic flux in Φ_0 at a given magnetic field in mG for the π-ring with an angle θ_2 = 272°. This ring is expected to show a half magnetic flux quantum offset. The figure on the right hand side shows the expected magnetic flux for the 0-ring with θ_2 = 332°. This ring is expected to show integer flux quantization. All steps are expected to show up at $n\Phi_0/A_\pi$ (left figure) or $\left(n+\frac{1}{2}\right)\Phi_0/A_0$ (right figure) as mentioned in equations (4.1) and (4.2). The double vertical lines at the jumps are due to an uncertainty of 1 μm in the inner radii r_Y and r_N of the YBCO/Nb ring resulting from the fabrication process.

The eventual measurements done in zero field are plotted as a number of (half-)integer magnetic flux quanta in the ring against the effective applied magnetic field. The resulting graph is shown for both the 0- ring and the π-ring in figure 4.2.

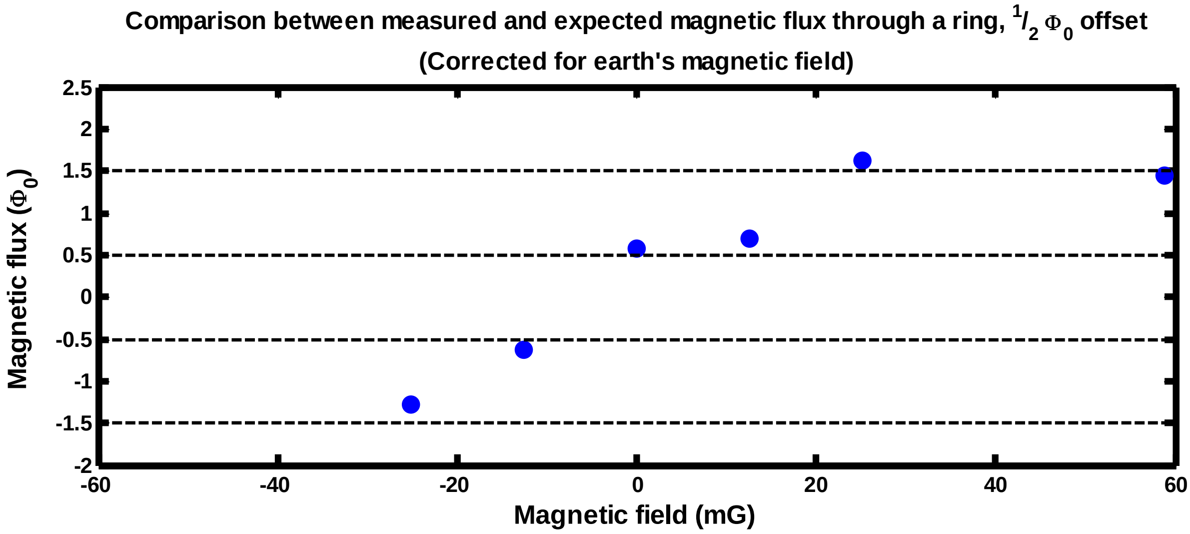

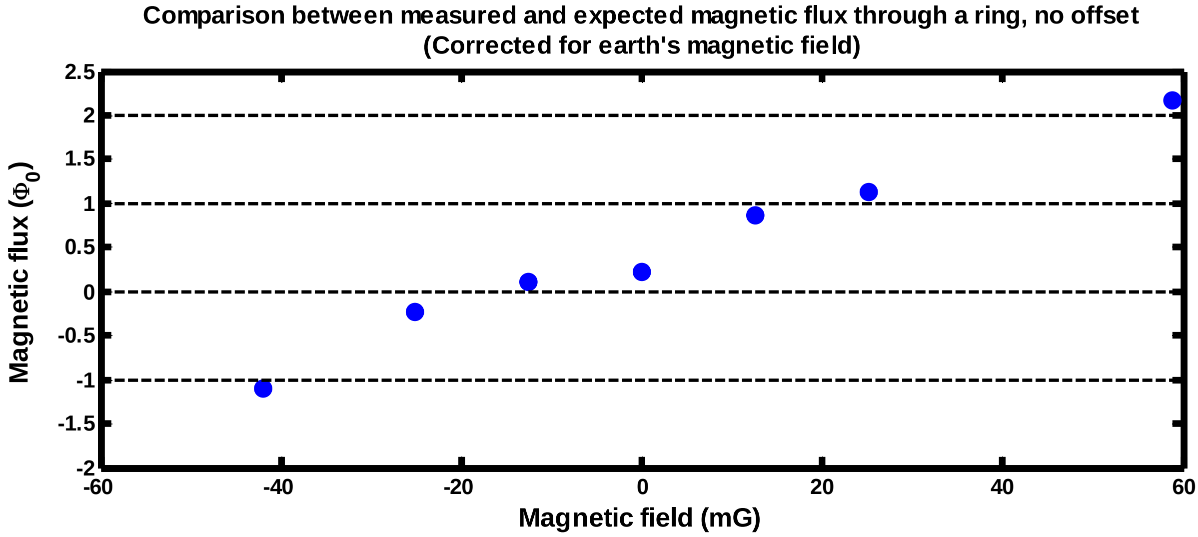

Figure 4.2: The upper figure shows the measured magnetic flux in Φ_0 at a given magnetic field in mG for the π-ring with θ_2 = 272°. The lower figure shows the magnetic flux in Φ_0 as a function of applied magnetic field in mG for the 0-ring with θ_2 = 332°. For both figures the following scaling holds. If the applied magnetic field value reads '0', this means that the earth's magnetic field is compensated for and no extra magnetic field is applied. For clarity, dashed horizontal lines are added to the graphs at half-integer and integer amounts of flux quanta respectively, since these are the only allowed states for the magnetic flux through the ring.

Flux profiles for the zero-field measurement are measured alongside the total flux scanning image. The profiles are extracted using Gwyddion version 2.31. An example of such a profile is shown in figure 4.3. By comparing the height of the peak seen in such a profile to a standardized peak height, an estimation of the flux through a ring can be made. The standard peak height has to be chosen for a ring with a known amount of flux quanta. This is best done for a π-ring that is cooled and measured without an external magnetic field, because the flux through this ring has to be $\pm\frac{1}{2}\Phi_0$. In this estimation, the height of the flux density peak in the center of the ring with respect to the flux density peaks on the ring is taken as a measure for the total flux through the ring. To make this comparison, it is important to take in all other important factors that can change between different measurements, for example the flux-to-voltage transfer Φ-to-V of the flux-locked loop and the scan step size $\sqrt{A_p}$.

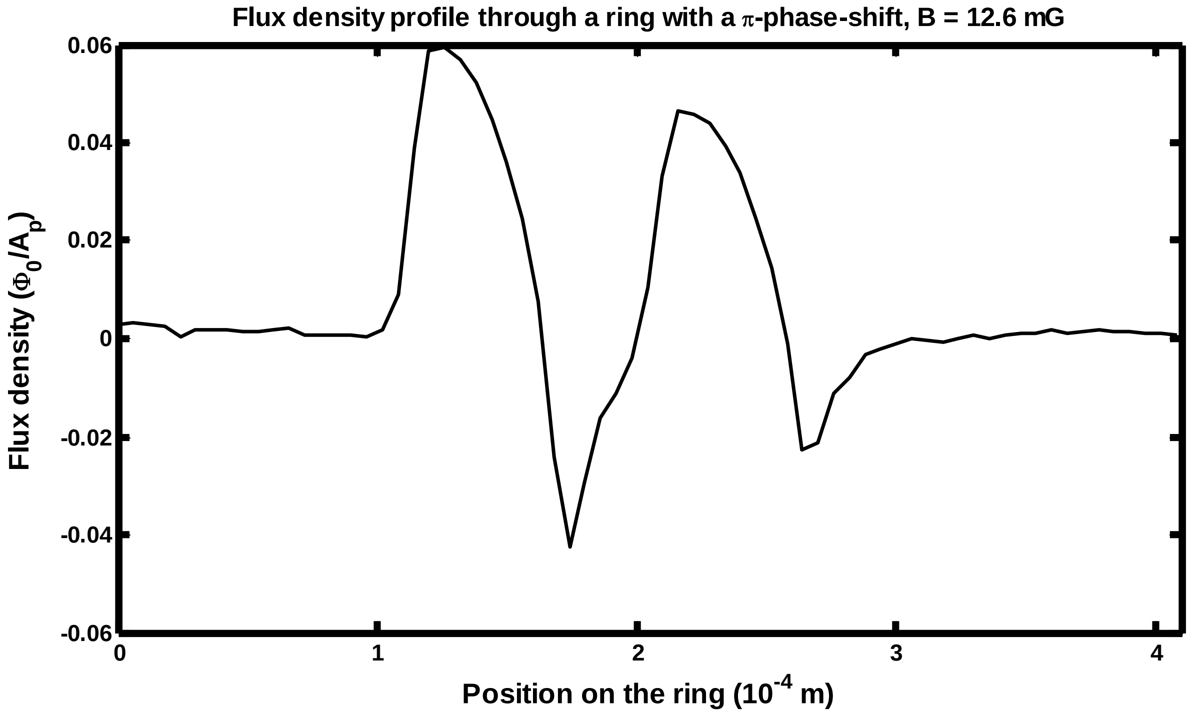

Figure 4.3: Flux density profile of the ring with a π-phase-shift (π-ring). This measurement is done with a current of 0.95 mA through the solenoid corresponding to a magnetic field of 12.6 mG during the cool-down of the sample. Three regimes that can be distinguished. Outside the ring, the flux density is zero because of the magnetic field being set to zero. On the ring, flux focusing plays an important role and a positive peak is observed. Inside the ring, flux quantization makes for a negative dip in the flux density.

An important feature of the profile shown in figure 4.3 is the small offset of the flux density. As is expected from a measurement done in zero magnetic field, the offset is small. An approximate calculation shows that this offset of $1.4 \cdot 10^{-3}\ \Phi_0/A_p$ corresponds to a residual magnetic flux density of 0.80 mG**.** This value is assumed small enough compared to the applied magnetic field to say that it is negligible.

4.3. Measurements conducted in field

The measurements in field are expected to show the same result as the measurements in zero field, shown in figure 4.1. In the case of zero-field measurements, the magnetic flux is trapped in the ring during the cool-down and should not change when the field is turned off. Then, this magnetic flux is caused by a circulating supercurrent I_s which has started to flow spontaneously in the ring. However, in the case of in-field measurements, a flux Φ_e applied by an external magnetic field is still present. Here, to keep the magnetic flux in the ring a smaller supercurrent I_s is needed according to equation (2.24). This smaller current results in a smaller chance that the Josephson junctions will break down due to the current exceeding the critical current I_c. So the expectation is that higher magnetic fields strengths and states with a higher (half-)integer number of magnetic flux quanta can be reached for in-field measurements.

The measurements conducted without an applied background field (zero-field measurements) do however give a stronger proof of the possible existence of the $1\frac{1}{2}\Phi_0$ state. The spontaneously generated current flowing through the superconducting ring and inducing the magnetic flux, should keep circulating even if the background field is turned off. So in this case, the ring should be able to fully sustain this $1\frac{1}{2}\Phi_0$ state without any help from an external magnetic field.

The results from the measurements done in an applied magnetic field are shown in figure 4.4.

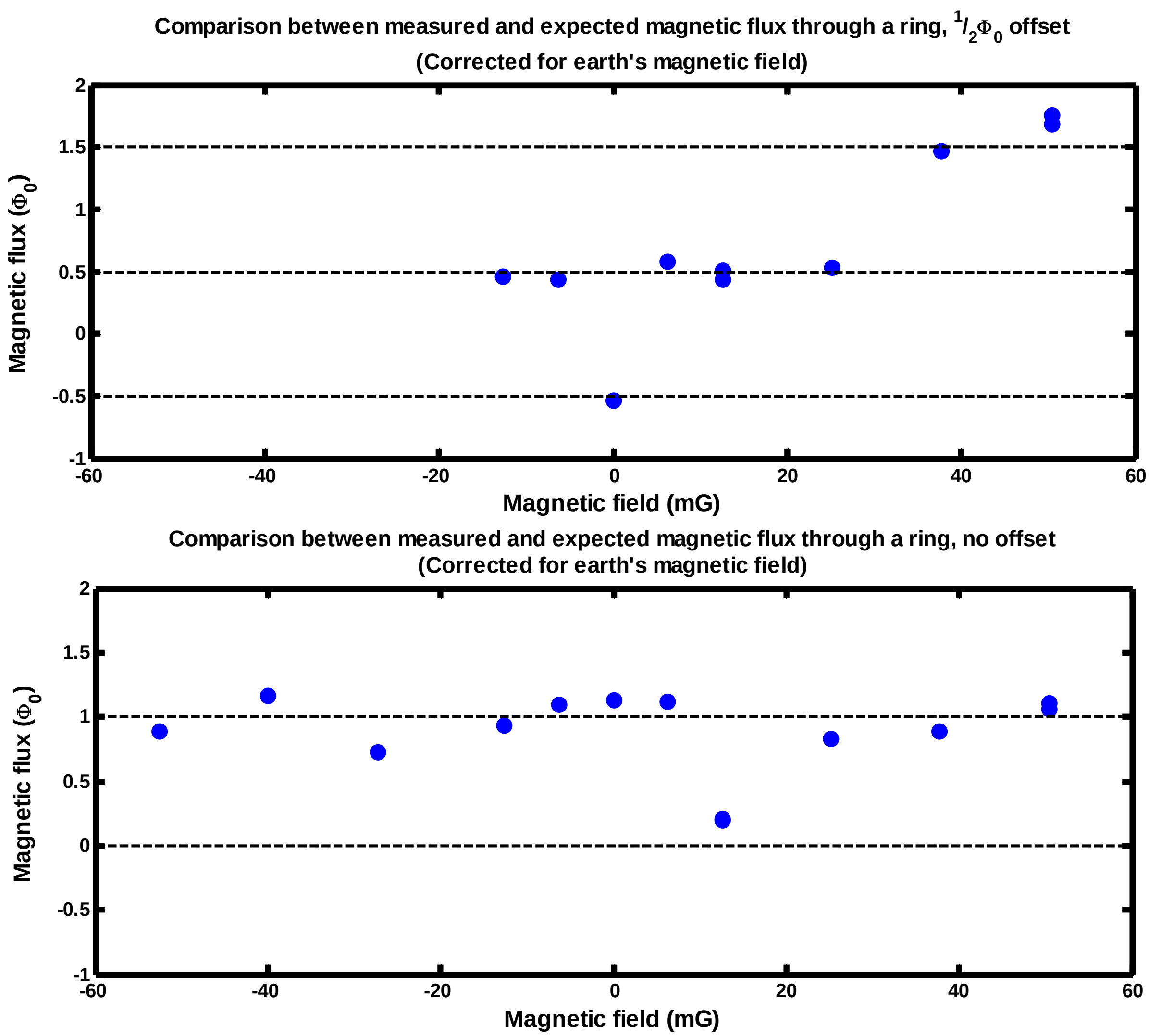

Figure 4.4: The upper figure shows the magnetic flux through the π-ring as a function of magnetic field. The lower figure shows the results for the same type of measurement, but here the

measurement is performed on the 0-ring. In both figures, dashed horizontal lines are added at the half-integer or integer numbers of flux quanta for clarity, since these are the only states allowed for the magnetic flux through the respective ring.

Profiles of the magnetic flux density are measured. A typical example of such a profile for the in-field measurements is shown in figure 4.5.

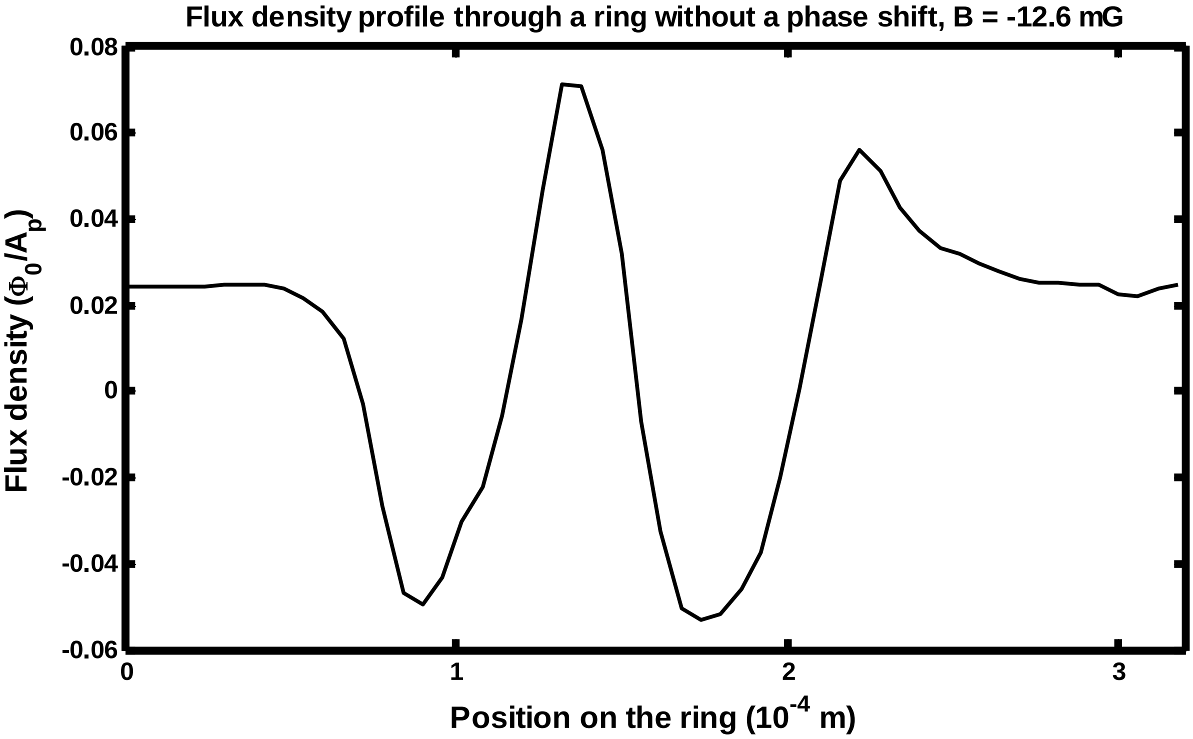

Figure 4.5: Flux density profile for a measurement performed on the ring without a π-phase-shift (0-ring). The current of −0.95 mA through the solenoid corresponds to a magnetic field of −12.6 mG. The flux density is plotted as a function of the position on the ring. The same three regimes as in figure 4.3 can be observed. Note that, because of the applied magnetic field during the measurement, the flux density outside the ring is not zero, but is offset to a positive value.

The magnetic flux through the 0- or π-ring that is estimated using the magnetic flux density profiles, generally deviates less than $0.1\Phi_0$ from the flux that is computed using Verwijs' program [21] to integrate the flux over all pixels within the inner radius of the ring. From this, the conclusion is drawn that the measurement data given in figures 4.2 and 4.4 is in good agreement with the flux density profiles given in figures 4.3 and 4.4 respectively.

Chapter 5. Discussion

5.1 Introduction

In this chapter, the results shown in chapter 4 will be discussed. This chapter will start with discussing the measurements done in zero magnetic field, followed by a discussion of the measurements done in non-zero field. After the measurement results for both measurement types have been discussed, the two types will be compared to each other in the last section of this chapter.

5.2 Discussion on measurements conducted in zero field

In figure 5.1, the magnetic flux values that were measured in zero magnetic field are compared to the expectations for these values.

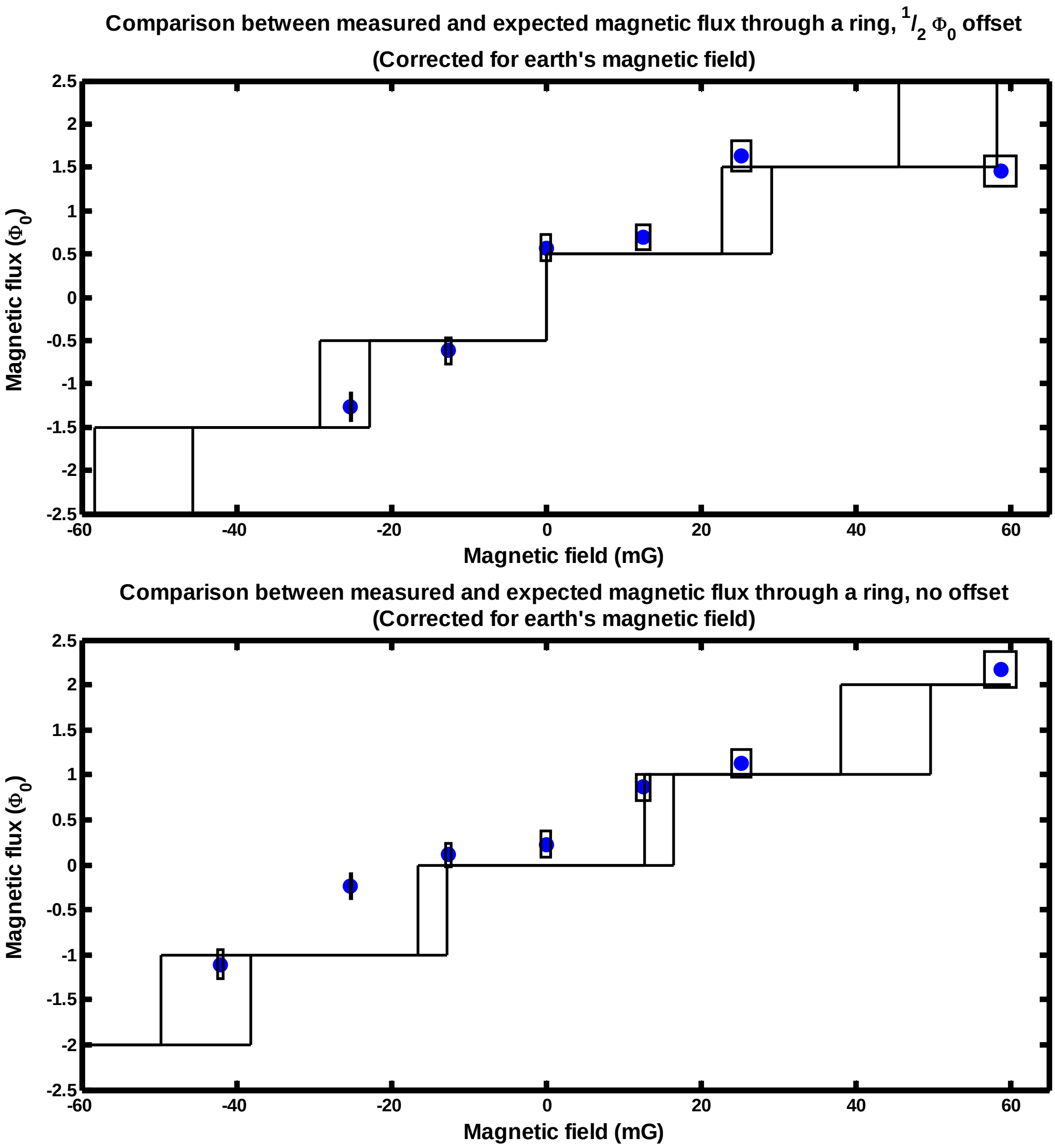

Figure 5.1: In the upper figure, the expected steps in magnetic flux are shown together with the measured values for magnetic flux through the π-ring. The lower figure is comparable, but the measurements are performed on the 0-ring. The measurements are done without a background field, but the scan head with sample and the SQUID stage are cooled down in the magnetic field

indicated on the x-axis in the (Φ,B)-diagrams. The separate graphs, not imposed on each other, are shown in figures 4.1 and 4.2. Error boxes are plotted to show the possible experimental errors $\Delta\Phi$ and ΔB in the magnetic flux Φ (in Φ_0) and the magnetic field strength in the z-direction B (in mG) respectively.

For both the 0- and π-ring, the main part of the measurements follow the expected pattern. Some deviations from this pattern are observed though. The error boxes for the measurements are calculated by incorporating the possible errors $\Delta\Phi$ and ΔB in the values of the magnetic flux Φ and the magnetic field strength B in the z-direction respectively.

Experimental errors in the total amount of measured flux through the ring Φ are mainly the result of possible deviations in the flux-to-voltage transfer Φ-to-V and the defined integration area (see equation (2.28) in section 2.4.3). The experimental error as a result of Φ-to-V is calculated using partial derivatives:

$$\Delta\Phi = \Delta\left(\sum_{r<R_{in}} \Phi_p\right) = \frac{\partial\left(\sum_{r<R_{in}} \Phi_p\right)}{\partial(\Phi - \mathrm{to} - \mathrm{V})}\Delta(\Phi - \mathrm{to} - \mathrm{V}) = \frac{\Delta(\Phi - \mathrm{to} - \mathrm{V})}{\Phi - \mathrm{to} - \mathrm{V}}\sum_{r<R_{in}} \Phi_p \tag{5.1}$$

The experimental error as a result of deviations in the defined integration area is estimated by computing $\Phi = \sum_{r<R_{in}} \Phi_p$ several times. From the values that are found in these calculations the possible deviation is estimated and applied in $\Delta\Phi$; this can be seen as accounting for possible deviation in $\sum_{r<R_{in}} N(r)^*$ (see equation (2.28)). So, in fact

$$\Delta\Phi = \left(\frac{\Delta(\Phi - \mathrm{to} - \mathrm{V})}{\Phi - \mathrm{to} - \mathrm{V}} + \frac{\Delta\left(\sum_{r<R_{in}} N(r)^*\right)}{\sum_{r<R_{in}} N(r)^*}\right)\Phi \tag{5.2}$$

It is assumed that $\Delta(\Phi - \mathrm{to} - \mathrm{V})$ is 0.3 V/Φ_0. The experimental errors Δgain, ΔA_p and ΔA_s in the gain, A_p and A_s (see equation (2.28)) respectively, turn out be negligible and are therefore omitted in the considerations above.

Possible deviations in the applied external magnetic field B with

$$B = C \cdot I \tag{5.3}$$

are the result of two factors: a constant experimental error in the calibration constant C and experimental errors in the current flowing in the solenoid I. Using partial derivatives the experimental error in B is found to be

$$\Delta B = C\Delta I + I\Delta C \tag{5.4}$$

where C is the calibration constant with a value of 42 G/A. ΔI and ΔC are estimated to be 0.01 mA and 0.5 G/A respectively.

When comparing the measurement points with error boxes to the expected quantized magnetic flux states in the rings, some deviation is still observed. A possible explanation for the deviations that are still present is that the ring contains corner junctions. Because the YBCO semi-rings were chosen wider than the niobium semi-rings, they do not match together precisely (see also figure 3.9 in section 3.5). The niobium is partly encompassed by the YBCO, introducing extra junctions in the ring. These junctions are relatively small but do introduce some extra spontaneously generated currents flowing in the ring.

Using the program described in section 2.5 and [18], mappings were made of the current flowing in the rings. Some examples of functioning rings where the junctions were not broken down are given in figure 5.2.

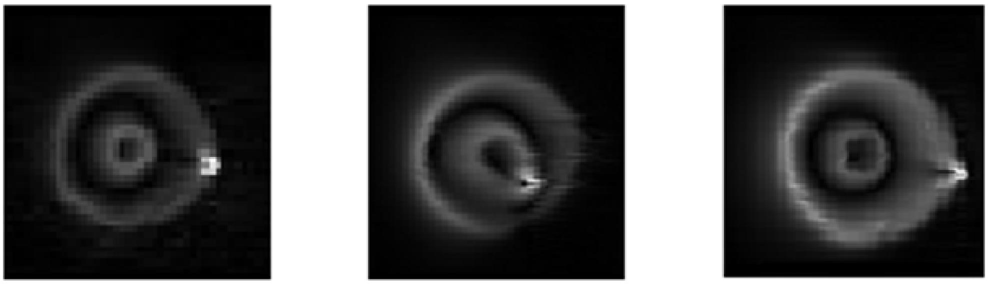

Figure 5.2: Mappings of the current density $|\mathbf{J}|$. A high current density is shown as a bright, white color. No current is shown as black. The bright white spots seen on the rings are vortices. In a vortex, one flux quantum Φ_0 is generated while the current can only circulate in a small loop. This results in a high current density around the vortex. As a result of the Meissner effect, all current is generally flowing on the edge of the ring, this way shielding the magnetic field out of the superconducting ring.

Since the superconducting rings are subject to the Meissner effect, they show zero magnetic flux density on the ring. This is best illustrated with a 3-dimensional plot, shown in figure 5.3.

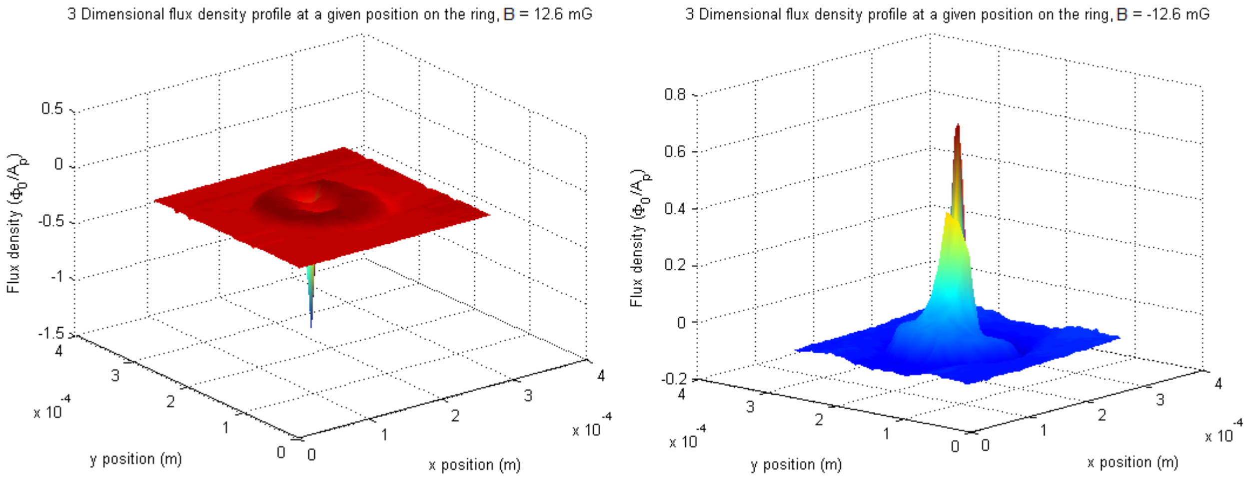

Figure 5.3: In the left figure, a 3-dimensional plot of the flux density profile of the π-ring is shown. The big negative spike on the ring is a vortex. This vortex is used for calibration of the effective area of the sensor pick-up loop A_s, as described in section 2.4.3, which was found to be 24.6 μm^2. The smaller dip in the center is the flux going through the ring. This measurement is done for B = 12.6 mG during the cool-down. The right figure shows another flux density profile through the π-ring. Here $B = -12.6$ mG. In both figures, the pixel area A_p is 36 μm^2. For these figures, the color scale is arbitrary, and only the axes values are to be used.

There are several cases where a Josephson junction or even a part of the superconducting material in the ring can transition to its normal state. This transition can be the result of the temperature exceeding the critical temperature or the magnetic field exceeding the critical magnetic field, as mentioned in section 2.2. A Josephson junction can also transition to its normal state when the current flowing through the junction exceeds a certain critical current. When this transition from the superconducting state to the normal state has happened we say that the junction has been *broken down*. When a junction has been broken down the current will not flow through the junction, but will flow back via the inner edge of the ring to its starting point on the outer edge. As a result, the current does not circulate in a closed loop; using Stokes' Theorem to get to equation (2.9) and choosing the right integration path to get to equation (2.13) is not allowed anymore. The result is that the flux through the ring is not necessarily quantized anymore. This behavior is only expected at high enough fields. When this happens, it is possible to see the current flowing back via the inner edge of the ring using the current mapping program.

In the measurements in zero magnetic field, complete junction *breakdown* is not observed, because the measurements were stopped when the junctions started to break down. This start of the breakdown of the junctions is shown in figure 5.4. In the figure it can be seen that a current is flowing across the junctions towards the inner edge of the ring. This implies that the junctions have been broken down. This breakdown can be explained by the high currents flowing in the ring. Since in this experiment the magnetic field is set to zero, all magnetic flux through the ring has to be generated by the current circulating in the ring. To generate this flux the current has reached a value that is higher than the critical current for that junction. Because the sample containing the rings is already more than five years old, it is possible that the junctions have deteriorated, for example by oxidation of the niobium to insulating NbO_x obtaining the required oxygen from the neighboring YBCO that degrades in this way, and as a result have a decreased critical current density of orders of magnitude [9]. The breakdown of the junctions cannot be explained by the temperature or the magnetic field being too high, because the temperature is set well below its critical value and the magnetic field was set to zero during the zero-field measurement set.

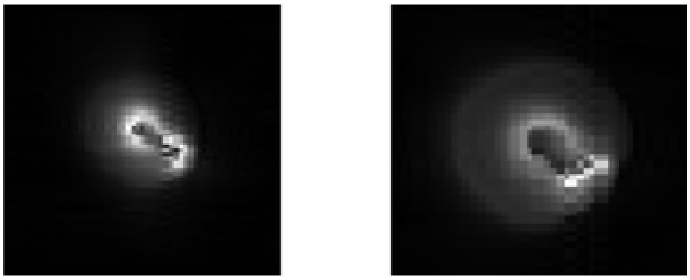

Figure 5.4: The start of the breakdown of the junctions. Current is still flowing through the junction, as can be seen from the white color in the junction area. But a part of the junction were already broken down. There is flux coming through the junctions. This means that the Meissner effect is not observed in these areas anymore and therefore part of the junction is not superconducting anymore.

The 3-dimensional flux density profiles also show this breakdown of the junction. Since the junction is not superconducting anymore, flux can go through the junction, as can be seen in figure 5.5.

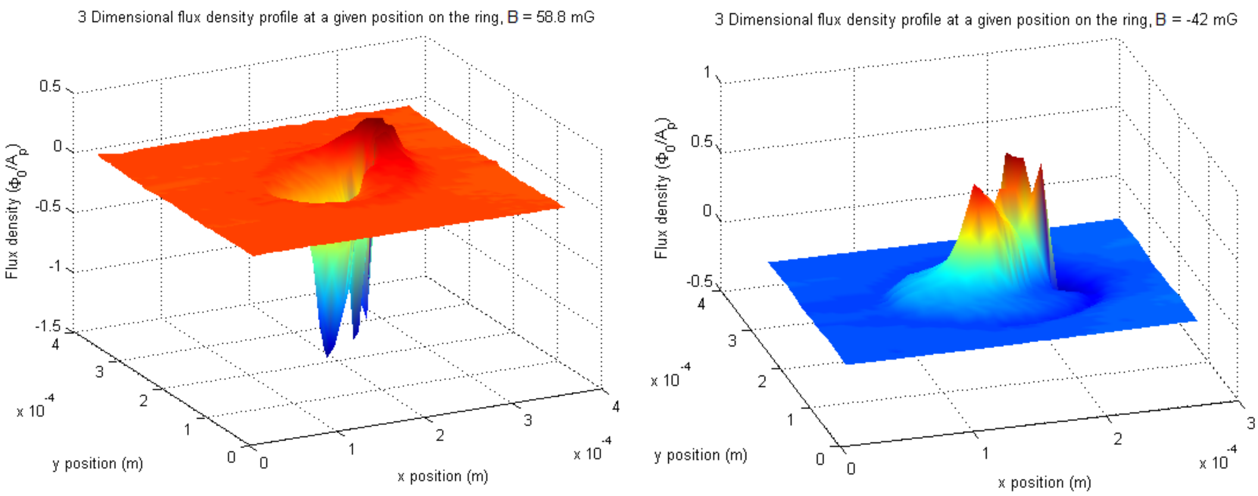

Figure 5.5: In both figures it can be seen that the junctions were broken down. Inside the junctions, magnetic flux can be seen. This is visible via a second peak next to the first expected peak. The breakdown of the junctions is a result of either currents exceeding the critical current or the

magnetic field exceeding H_{c2}. For these figures, the color scale is arbitrary, and only the axes values are to be used.

This breakdown of the junctions is a possible explanation of the deviations between measured and expected flux, shown in figure 5.1 in this section. The quantization condition is not fully met and therefore the flux stays close to its quantized value, but is not exactly equal to it. The expectation is that flux deviates more from the expected quantized value as fields get higher until at some magnetic field strength a step in the (half-)integer number of flux quanta is reached. This still results in a step in the measured amount of flux up to the next (half-)integer number of flux quanta. Raising the field strength even further should then again give rise to deviations from the expected value.

The deviation from the expected magnetic flux state might also be explained by an exited energy state. When computing the expected values for magnetic flux, it is always assumed that the magnetic flux is quantized to its energetically most favorable state, the ground state which has the lowest energy. This type of energy minimization is often seen in physical systems. This does not mean that the energetically most favorable state is the only state that can be occupied. There is a chance that higher (excited) energy states are occupied, even though the probability of this happening is assumed to be smaller than the probability of the (ground) state with minimal potential energy being occupied. This cause for deviations from the expected quantized magnetic flux state can explain why the flux still seems to be quantized.

5.3 Discussion on measurements conducted in field

The measured values for the magnetic flux are plotted as a function of the applied magnetic field in figure 5.6, as done for the measurements in zero field in figure 5.1.

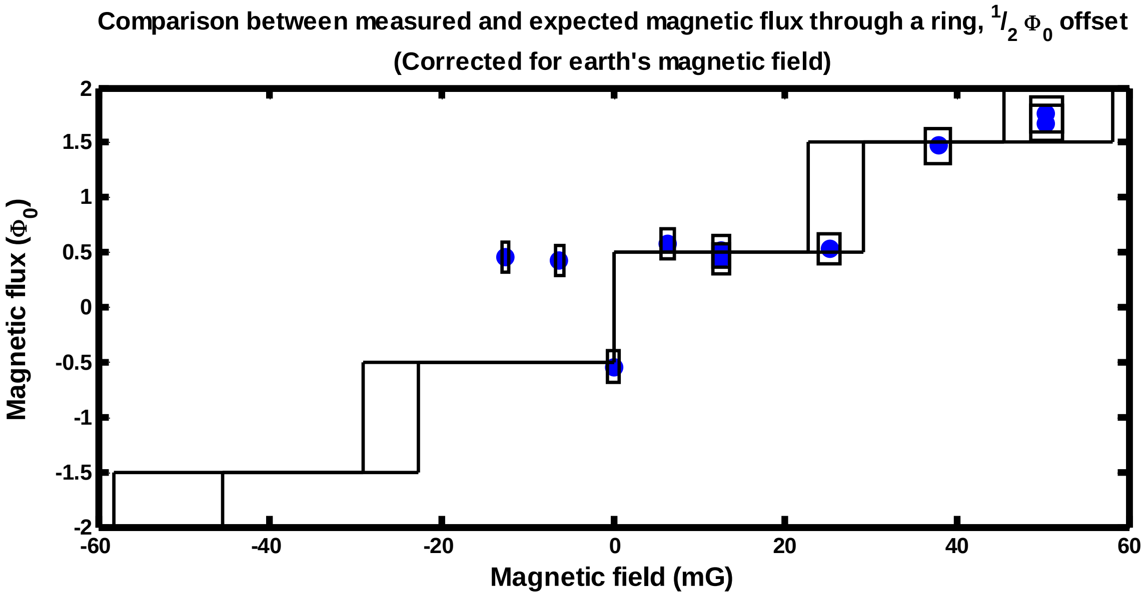

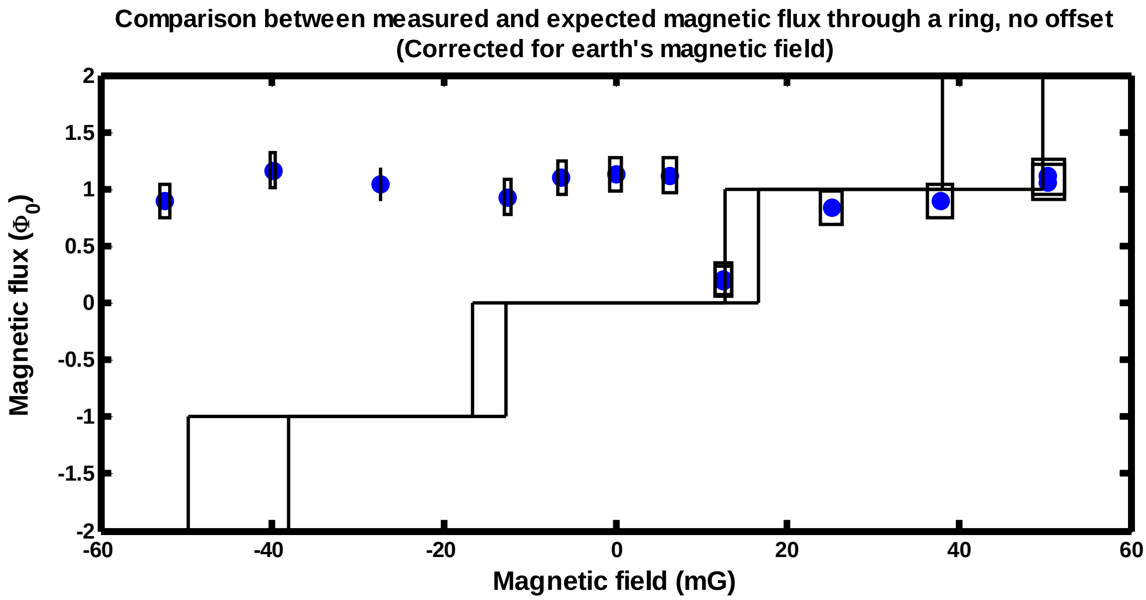

Figure 5.6: In the upper figure, the expected steps in magnetic flux are shown together with the measured values for magnetic flux in the π-ring. The lower figure is comparable, but the measurements were performed on the 0-ring. The measurements were conducted in a background field. The cool-down is done in the same background field. The separate graphs, not imposed on each other, are shown in figures 4.1 and 4.4.

In the upper figure in figure 5.6 for the π-ring, it can be seen that although negative magnetic flux is expected for negative magnetic field strengths, the measured magnetic flux is positive. The only negative point seen in this figure is at effectively $B = 0$ mG. The expected step from the $½\Phi_0$ state to the $1½\Phi_0$ state is observed for the magnetic field strength that was hypothesized in chapter 4.

In the lower figure in figure 5.6 for the 0-ring, the same problem arises as for the measurements done on the π-ring. All measured values for the magnetic flux are positive. Another problem that arises in this figure is that where the expectations were that the flux would be 0 or $-1\Phi_0$, the measured flux is still $+1\Phi_0$. For these measurements done on the 0-ring, the deviations from the expected magnetic flux cannot all be explained by the chance that the higher excited potential energy states are occupied. Since this effect is statistical it is not expected that it happens as many times as is seen in this in-field 0-ring measurement series.

For this series of in-field measurements, there are also mappings of the current density. Some mappings for well functioning rings are shown in figure 5.7.

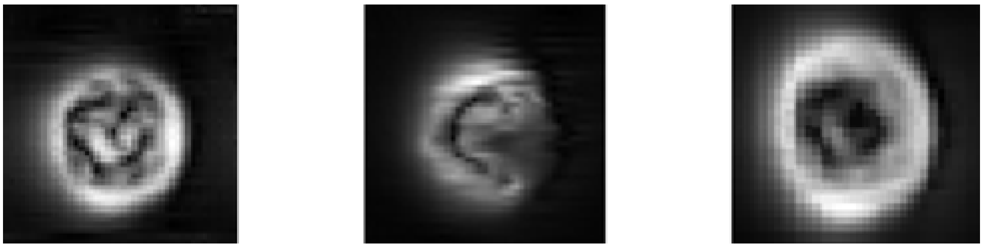

Figure 5.7: Some examples of the current in a ring when spontaneously generating a magnetic flux. The figures show high values of the current density $|\mathbf{J}|$ in white while zero values of $|\mathbf{J}|$ are shown as black. It can be seen that the currents are generally flowing on the edges of the ring as expected by the Meissner effect. Currents inside the ring are generally vortices. In these figures, the current circulates all the way around the ring.

Examples of the 3-dimensionally plotted flux density profiles of such well-functioning rings are shown in figure 5.8.

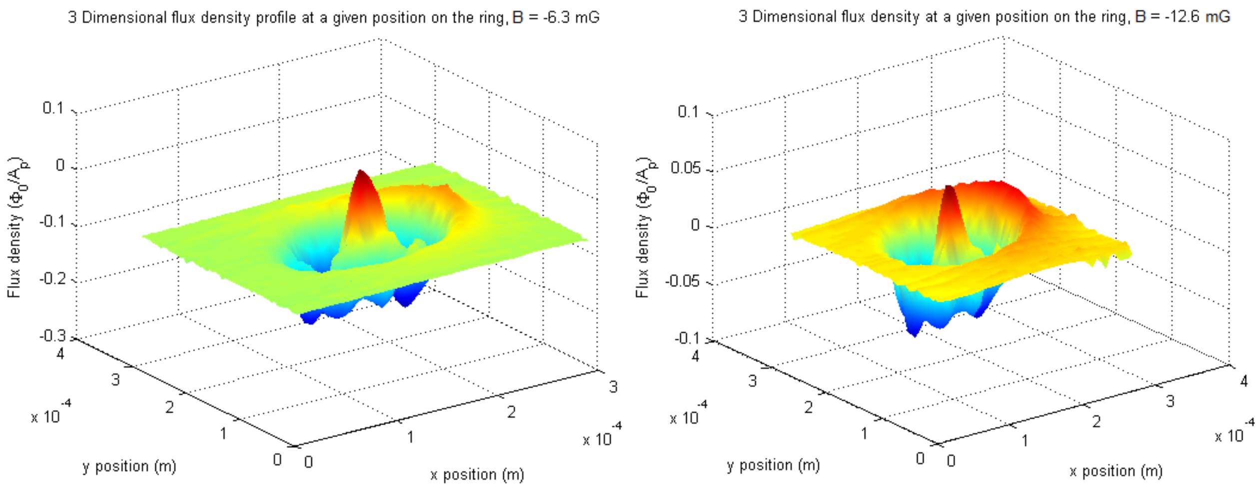

Figure 5.8: These figures show the flux density profiles for rings where the junctions were not broken down. For these figures, the color scale is arbitrary, and only the axes values are to be used.

Some of the junctions were broken down during the measurements. A few examples of these junctions are shown in figure 5.9. In the figure the broken-down junctions can be seen by the current flowing across the junction towards the inner edge of the ring, as in figure 5.4. The difference with the measurements in figure 5.4 is that the field is not set to zero this time. The externally applied magnetic field now produces part of the magnetic flux through the ring. The only supercurrent flowing through the ring is a current to round the (half-)integer number of flux quanta to its nearest quantized value. This current is low enough to not exceed the critical current of the junction. The magnetic field that is used can be the cause of the junction breakdown. If the magnetic field that is used exceeds the critical magnetic field of the junction, superconductivity is suppressed in the niobium. This results in the current flowing back via the inner edge of the ring, as can be seen in figure 5.9. In any case, it is not the critical external magnetic field H_{c2} of niobium that is exceeded, because this critical field is of an order of magnitude of 10^3 G = 10^{-1} T at a temperature of 4.2 K [22], while the highest external magnetic field that was used in the experiments is lower than 60 mG = $6.0 \cdot 10^{-6}$ T.

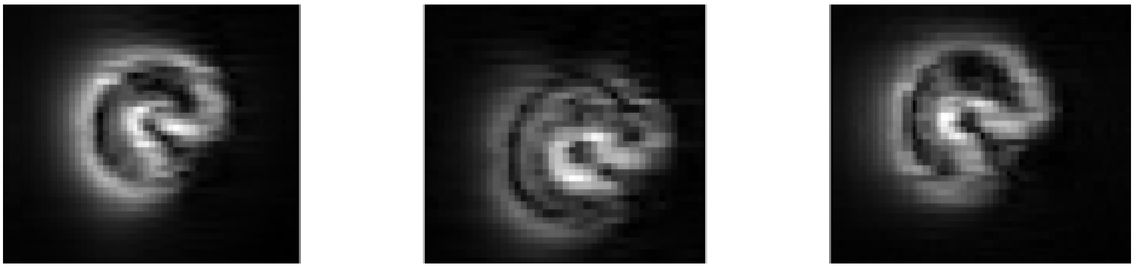

Figure 5.9: In the above figures, junction breakdown due to the exceeding of the critical current is shown. All three pictures show that no current flows between the two junctions in the ring, but current actually flows along, or parallel to, the junctions. The current flows back via the inner edge of the ring and forms a closed loop that does not include the superconducting ring itself.

Flux density profiles for some rings with broken down junctions are shown in figure 5.10.

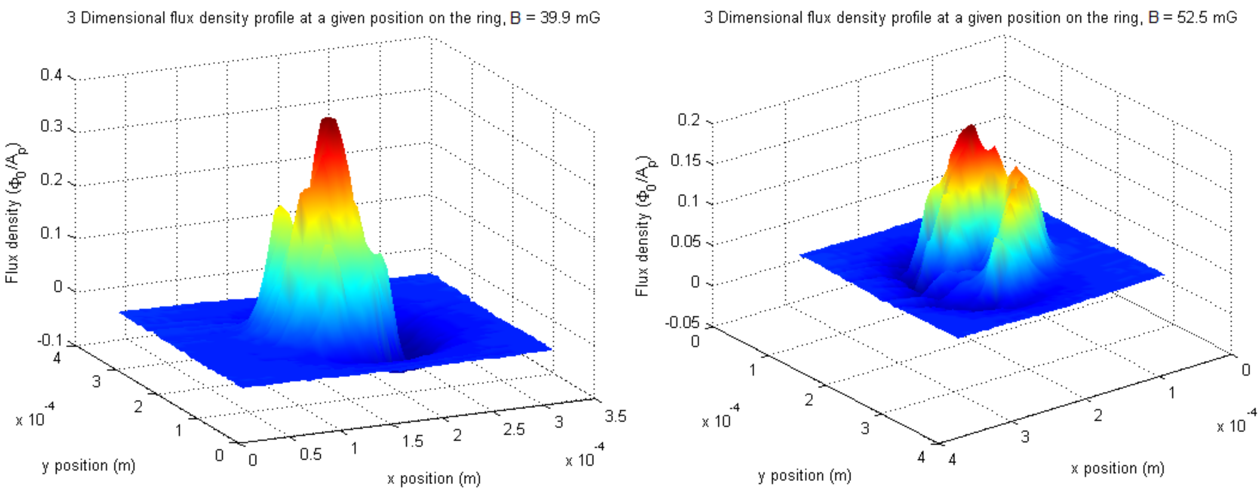

Figure 5.10: This figures show two measurements on rings with broken down junctions. It can be seen that there is some positive flux inside the junctions, which means that the junctions are not superconducting anymore. For these figures, the color scale is arbitrary, and only the axes values are to be used.

The expectation was that for the in-field measurements the breakdown of the junctions would happen at higher magnetic field strengths than for the zero-field measurements. This is because of the externally applied flux during the scanning of the rings. Flux that is already applied on the ring does not have to be generated by supercurrents spontaneously flowing in the ring. This results in a lower current and therefore a lower chance of exceeding the critical current of the junctions.

Comparing figure 5.6 to figures 5.9 and 5.10, it clearly turns out that although the junctions were broken down, the measured flux is still shown to be quantized inside the rings. This is not completely unexpected, as the part of the ring that is not superconducting anymore is relatively small compared to the part that is still superconducting. This means that using Stokes' Theorem to get to equation (2.9) is not exact anymore, but using it is still approximately justified. An analogous argument holds for the choice of the integration path to get to equation (2.13). The largest part of the integration path, the part inside the superconducting region of the ring, still shows $\mathbf{J}_s = \mathbf{0}$. Only a small part, the non-superconducting region, will have a finite value for $\mathbf{J}_s$. When the non-superconducting part of the ring becomes larger, it is expected that the flux quantization condition will no longer hold.

5.4 Comparing the in-field and zero-field results

Contrary to what one would expect, it was not possible to measure higher (half-)integer magnetic flux quantum states in the in-field measurement series than in the zero-field measurements series. The junctions broke down before the high (half-)integer numbers of flux quanta were reached. It is possible that this is due to the applied magnetic field getting closer to the critical magnetic field H_{c2} of the ramp-type Josephson junctions via which the YBCO/Nb rings are connected. If a higher magnetic field while measuring is a cause of a lower critical current, this may explain why the junctions broke down before the higher flux quantum states seen in the zero-field measurements series, were reached. Future research might point out whether this hypothesis is correct.

As implicitly mentioned at the start of this section, it is also expected that the supercurrent flowing in the ring in the zero-field measurements series is higher than in the in-field measurements series. But because of the rather precise need for calibration in the program for mapping the current density in the ring, it is not possible to observe this.

Chapter 6. Conclusions and recommendations

The main goal of this bachelor assignment was either experimentally observing the $1½\Phi_0$ state of either positive or negative polarity in a high-T_c/low-T_c superconducting ring with a π-phase-shift or explaining why it cannot be experimentally observed. This goal has been achieved. The $\pm1½\Phi_0$ state has been measured in both measurements performed without any magnetic field and measurements performed in a magnetic field.

As an experimental check, the steps in the half-integer number of magnetic flux quanta in the π-ring have been measured. For the measurements conducted without a background field, the measured data showed only a minimal deviation from the expected values. For the measurements performed in a background field, this deviation was larger. In the case of the ring without π Josephson junctions (0-ring), almost every measured flux value, with only one exception, showed a positive amount of flux i.e. the $+1\Phi_0$ state. This does not agree with the theoretical expectation that negative magnetic field gives rise to negative magnetic flux in the ring. It has to be noted that an important feature, the step between the $½\Phi_0$ state and the $1½\Phi_0$ state, was measured in the in-field measured π-ring.

Future research might be done on superconducting rings scanned in a background magnetic field using scanning SQUID microscopy. Our measurements showed that the flux states in the rings did not follow the steps that might be expected from the 0- and π-ring for the in-field measurement series. New measurements should be done to see if this has only an experimental reason, or if something more fundamental governs the flux in these in-field measurements.

The superconducting rings in zero magnetic field also showed some deviations from the expected values that could not be explained in this thesis. Future research might point out the cause of these deviations.

The deviation from the expected magnetic flux state might be explained by an exited energy state. There is a chance that higher excited energy states are occupied, even though the probability of this happening is assumed to be smaller than the probability of the ground state with minimal potential energy being occupied. This cause for deviations from the expected quantized magnetic flux state can explain why the flux still seems to be quantized in the cases of deviation in the zero-field 0-ring measurement set (one deviation) and the in-field π-ring measurement set (two deviations). The excited energy magnetic flux state explanation is not applicable on the in-field 0-ring measurement set since there are too many deviations that show the excited $+1\Phi_0$ state.

For future research, it is also interesting to look at the breakdown of the Josephson junctions in the 0- and π-ring. As is stated at the end of section 5.3 the expectation was that for measurements performed in a magnetic field, the junctions would break down for higher magnetic field strengths as compared to zero-field measurements. The experiments, using the current density mapper, showed the contrary. The junctions, when subject to an external magnetic field, broke down for even lower magnetic field strengths than the junctions without an externally applied field during the measurement. In section 5.2 we hypothesized that the breakdown of the junctions might give rise to the deviations from the expected steps in the allowed (half-)integer magnetic flux quantum states. This hypothesis can be checked by using scanning SQUID microscopy and possibly the program for mapping the current density in the rings.

The next step in research on superconducting loops would be a form of superconducting quantum-electronical circuits. Using the resistanceless conduction in superconductors, energy can be transported without or with only minimal losses. Knowledge on the behavior of magnetic fields and magnetic flux in these circuits is vital to the working of these systems.

Acknowledgements

This thesis has had great benefit from the support of a lot of people. We would like to thank some of these people here.

First, we are very grateful to professor Hilgenkamp for his advice on our research and for offering the very interesting topic of research.
Xiao Renshaw Wang and Steven Wells have helped us a lot during the course of this project. You have learned us a lot on operating the SSM and we were always able to turn to you if we had any questions.

Finally, we would like to thank everyone in the ICE group for the great time we have had here. It has been a lot of fun working with all of you for the past months.

References

[1] J.R. Kirtley, C.C. Tsuei, Ariando, C.J.M. Verwijs, S. Harkema and H. Hilgenkamp, *Angle-resolved phase-sensitive determination of the in-plane gap symmetry in $YBa_2Cu_3O_{7-\delta}$*, Nature Physics, 2006, vol. 2, 190-194.

[2] M. Tinkham, *Introduction to superconductivity*, 2nd ed., McGraw-Hill, (1996).

[3] J.G. Bednorz and K.A. Müller, *Possible high T_c superconductivity in the Ba-La-Cu-O system*, Zeitschrift für Physik B, 1986, vol. 64, 189-193.

[4] J. Bardeen, L.N. Cooper and J.R. Schrieffer, *Microscopic theory of superconductivity*, Physical Review, 1957, vol. 106, 162-164.

[5] J. Bardeen, L.N. Cooper and J.R. Schrieffer, *Theory of superconductivity*, Physical Review, 1957, vol. 108, 1175.

[6] S. Lundqvist, *Nobel lectures in physics 1971 – 1980*, World Scientific Publishing, (1992).

[7] W. Meissner and R. Ochsenfeld, *Ein neuer Effekt bei Eintritt der Supraleitfähigkeit*, Die Naturwissenschaften, 1933, vol. 21, 787-788.

[8] V.L. Ginzburg and E.A. Andryushin, *Superconductivity*, World Scientific Publishing, Singapore, (1994).

[9] C.J.M. Verwijs, *Fractional flux quanta in high-T_c/low-T_c superconducting structures*, Ph.D. Thesis, University of Twente, (2009).

[10] S. Gasiorowicz, *Quantum physics*, 3rd ed., Wiley-VCH, (2003).

[11] V.L. Ginzburg and L.D. Landau, *Phenomenological theory of superconductivity*, Zh. Eksp. Teor. Fiz., 1950, vol. 20, 1064.

[12] B.S. Deaver jr. and W.M. Fairbank, *Experimental evidence for quantized flux in superconducting cylinders*, Physical Review Letters, 1961, vol. 7, 43-46.

[13] D.J. Griffiths, *Introduction to electrodynamics*, 3rd ed., Pearson Benjamin Cummings, San Francisco, (2008).

[14] B.D. Josephson, *Supercurrents through barriers*, Advances in Physics, 1965, vol. 14, 419-451.

[15] J. Clarke and A.I. Braginski, *The SQUID handbook vol. I fundamentals and technology of SQUIDs and SQUID systems*, Wiley-VCH Verlag, (2004).

[16] J. Clarke and A.I. Braginski, *The SQUID handbook vol. II applications of SQUIDs and SQUID systems*, Wiley-VCH Verlag, (2006).

[17] J.R. Kirtley, M.B. Ketchen, K.G. Stawiasz, J.Z. Sun, W.J. Gallagher, S.H. Blanton and S.J. Wind, *High-resolution scanning SQUID microscope*, Applied Physics Letters, 1995, vol. 66, 1138-1140.

[18] F. Laviano, D. Botta, A. Chiodoni, R. Gerbaldo, G. Ghigo, I. Gozzelino, S. Zannella and E. Mezetti, *An improved method for quantitative magneto-optical analysis of superconductors*, Superconducor Science and Technology, 2003, vol. 16, 71-79.

[19] Ariando, *Josephson junction arrays with d-wave-induced π-phase-shifts*, Ph.D. Thesis, University of Twente, (2005).

[20] T. Wijnands, *Scanning superconducting quantum interference device microscopy*, Master Thesis, University of Twente, (2013).

[21] C.J.M. Verwijs, *Scanning SQUID microscope soort van gebruiksaanwijzing*, (2010).

[22] K. Saito, *Critical field limitation of the niobium superconducting RF cavity*, KEK Accelerator Lab, Ibaraki-ken, 10th International SRF Workshop, Japan, (2001).

Appendix A. Fractional flux quantization by energy minimization

A.1 Energy in a superconducting loop

This appendix gives a derivation of half-integer flux quantization by means of energy minimization as an alternative for the derivation that was done in section 2.3.5. This derivation might also give a more intuitive grasp of the spontaneous current that is generated to induce the half flux quantum. As such, this appendix can be thought of as the remainder of the consideration of half-integer flux quantization in chapter 2.

The total energy of the superconducting loop and the junctions is given by the electrical energy stored in the junctions and the generated magnetic field. The energy stored in a junction can be found by integrating the work needed to change the phase across the junction with respect to time, so

$$U_J = \int_0^t I_s V_J dt \tag{A.1}$$

where U_J is the energy stored in a junction and V_J is the voltage over a junction. I_s is the supercurrent through a junction, which can be found using equation (2.19). The voltage over a junction is given by[14]

$$V_J = \frac{\Phi_0}{2\pi}\frac{d\varphi}{dt} \tag{A.2}$$

Substituting (2.19) and (A.2) into equation (A.1) yields

$$U_J = \frac{\Phi_0 I_c}{2\pi}\int_{\varphi_0}^{\varphi} \sin(\varphi)\frac{d\varphi}{dt}dt = E_J(1-\cos\varphi) \tag{A.3}$$

where the integration constant was chosen to give $U_J = 0$ for $\varphi = 0$. The constant E_J is the so called *coupling energy* of the Josephson junction

$$E_J \equiv \frac{\Phi_0 I_c}{2\pi} \tag{A.4}$$

The energy stored in the magnetic field generated by the current through the superconductor can be seen as the energy of the magnetic field generated by a solenoid with the same magnetic induction L. This energy can be found by integrating the power with respect to time:

$$U_B = \int_0^t I_s V_J dt = \int_0^{I_s} L I_s' dI_s' = \frac{1}{2} L I_s^2 \tag{A.5}$$

The total energy in the superconducting loop is the sum of (A.3) for all junctions and (A.5). If two a loop contains two junctions with phases φ_1 and φ_2, this implies

$$U_l = U_J + U_B = E_{J1}(1-\cos\varphi_1) + E_{J2}(1-\cos\varphi_2) + \frac{1}{2}LI_s^2 \tag{A.6}$$

where U_l is the energy stored in the superconducting loop.

We use conservation laws to invoke the condition that the current should be the same through both junctions. This can be written as

$$I_s = I_{c1}\sin\varphi_1 = I_{c2}\sin\varphi_2 \tag{A.7}$$

We can find expressions for φ_2 as a function of a given φ_1 and the critical currents through both junctions:

$$\varphi_2 = \arcsin\left(\frac{I_{c1}}{I_{c2}}\sin\varphi_1\right) \tag{A.8a}$$

or

$$\varphi_2 = \pi - \arcsin\left(\frac{I_{c1}}{I_{c2}}\sin\varphi_1\right) \tag{A.8b}$$

If we substitute (A.8a) and (A.8b) into equation (A.6) and compute the energy difference the result is

$$U_l(\varphi_{2b}) - U_l(\varphi_{2a}) = \frac{\Phi_0}{\pi}\sqrt{I_{c2}^2 - I_s^2} \tag{A.9}$$

where we have used the identity $\cos(\sin^{-1} X) = \sqrt{1 - X^2}$. To get to this result, we have implicitly assumed that $I_{c2} \geq I_{c1}$. This assumption is justified because the indices 1 and 2 are arbitrarily chosen, so the two can be interchanged without any loss of generality. The difference in energies shown in equation (A.9) is always positive. This means that the energy stored in the loop is greater for solution (A.8b) than for solution (A.8a). So to minimize energy, it is always favorable for the phase of a junction to satisfy equation (A.8a).

A.2 Spontaneous current by energy minimization

Using this, consider a loop with 2 Josephson junctions with phases $\varphi_1 = \pi$ and $\varphi_2 = 0$ respectively. Now it is impossible for both junctions to satisfy equation (A.8a) with respect to each other and keep the phase difference π intact. So it should be impossible to minimize the energy in the system. Because the energy in the system cannot be minimized by the energy in the Josephson junctions, the loop is called a *frustrated loop*. This problem can be solved by adding a phase gradient $\nabla\varphi$. This would mean that the phase difference between the junctions would still be π while the phases in the junctions are still a solution to equation (A.8a). This would result in minimization of the energy in the loop.

Physically, a phase gradient in the loop would mean a current flowing through the loop, inducing a spontaneous magnetic flux. This spontaneous magnetic flux is the ½Φ_0 offset in the magnetic flux through the loop in equation (2.23).